# Silicon-Organic Hybrid (SOH) Mach–Zehnder Modulators (MZM) for Single-Carrier IM/DD Line Rates of 500 Gbit/s and Beyond

Adrian Schwarzenberger, Alexander Kotz, Dengyang Fang, Hend Kholeif, Carsten Eschenbaum, Lukas Grünewald, Christoph Wilhelm, Stefan Singer, Mohamed Kelany, Cheng Feng, Malte Martens, Adrian Mertens, Sidra Sarwar, Patrick Kern, Masis Sirim, Peter Erk, Artem Kuzmin, Yolita M. Eggeler, Stefan Bräse, Sebastian Randel, Wolfgang Freude, and Christian Koos

***Abstract*—Compact high-speed electro-optic modulators are key to next-generation optical transceivers for exa-scale data centers and large-scale artificial-intelligence (AI) clusters. As key performance metrics, the devices must combine large modulation bandwidth and low optical loss with compactness and low-voltage operation, while being amenable to efficient mass production, ideally on the silicon photonic platform. In this paper, we demonstrate silicon-organic hybrid (SOH) Mach-Zehnder modulators (MZM) that offer line rates in excess of 500 Gbit/s via low-complexity intensity-modulation-and-direct-detection (IM/DD) schemes. With $\pi$-voltage-length products $U_\pi L$ of only 0.67 Vmm, our devices combine efficiency and compactness, while being amenable to monolithic co-integration with a rich portfolio of proven silicon photonic devices. In a series proof-of-concept experiments, we demonstrate an SOH MZM with 280 µm-long phase-shifter sections, offering a 3-dB bandwidth of 74 GHz and a 6-dB bandwidth beyond 110 GHz along with a sub-1 dB phase-shifter loss. We achieve a PAM4 symbol rate of 204 GBd (line rate of 408 Gbit/s) and a PAM8 symbol rate of 176 GBd (line rate of 528 Gbit/s) – record values for MZM on the silicon photonic platform. We believe that our devices offer a highly attractive route towards next-generation optical transceivers with unprecedented efficiency and scalability. © 2025 The Author(s).**

***Index Terms*—Optical devices, optical fiber communications, integrated optics, electro-optic modulators, silicon photonics, optical interconnections, intensity modulation.**

This work was supported in part by the ERC Consol-idator Grant ‘TeraSHAPE under Grant 773248, in part by the DFG Excellence Cluster 3D Matter Made to Order under Grant EXC-2082/1–390761711, in part by DFG Collaborative Research Center HyPERION under Grant 454252029, in part by DFG Projects PACE under Grant 403188360, in part by GOSPEL under Grant 403187440, in part by the EU projects DYNAMOS under Grant 101070342, in part by ELLIPTIC under Grant 101187515, in part by CombTools under Grant 101136978, in part by CIELO under Grant 101187231, in part by BMBF Projects Open6GHub under Grant 16KISK010, in part by INTERSOUL under Grant 16KISK244K, in part by the MaxPlanck School of Photonics (MPSP), and in part by the Karlsruhe School of Optics & Photonics (KSOP).
*(Corresponding author: Adrian Schwarzenberger.)*

Adrian Schwarzenberger, Christoph Wilhelm, Stefan Singer, and Peter Erk are with the Institute of Photonics and Quantum Electronics (IPQ), Karlsruhe Institute of Technology (KIT), 76131 Karlsruhe, Germany, and also with the SilOriX GmbH, 76131 Karlsruhe, Germany (e-mail: adrian.schwarzenberger@kit.edu).

Alexander Kotz, Dengyang Fang, Mohamed Kelany, Sebastian Randel, and Wolfgang Freude are with the IPQ, KIT, 76131 Karlsruhe, Germany.

Hend Kholeif and Artem Kuzmin are with the IPQ, KIT, 76131 Karlsruhe, Germany, and also with the Institute of Microstructure Technology (IMT), KIT, 76344 Eggenstein-Leopoldshafen, Germany.

Carsten Eschenbaum, Cheng Feng, Malte Martens, and Adrian Mertens are with the SilOriX GmbH, 76131 Karlsruhe, Germany.

Lukas Grünewald was with the Laboratory of Electron Microscopy (LEM), KIT, 76131 Karlsruhe, Germany. He is now with the Institute for Anatomy and Cell Biology, University Freiburg, 79104 Freiburg, Germany.

Sidra Sarwar is with the IMT, KIT, 76131 Karlsruhe, Germany, and also with the Institute of Organic Chemistry (IOC), KIT, 76131 Karlsruhe, Germany.

Patrick Kern and Masis Sirim are with the IOC, KIT, 76131 Karlsruhe, Germany, and also with the Institute of Biological and Chemical Systems – Functional Molecular Systems (IBCS-FMS), KIT, 76344 Eggenstein-Leopoldshafen, Germany.

Yolita M. Eggeler is with the LEM, KIT, 76131 Karlsruhe, Germany. Stefan Bräse is with the IOC, KIT, 76131 Karlsruhe, Germany, and also with the IBCS-FMS, KIT, 76344 Eggenstein-Leopoldshafen, Germany.

Christian Koos is with the IPQ, KIT, 76131 Karlsruhe, Germany, and with the IMT, KIT, 76131 Karlsruhe, Germany, and also with the SilOriX GmbH, 76131 Karlsruhe, Germany (e-mail: christian.koos@kit.edu).

## I. Introduction

TRAINING of large-scale artificial-intelligence (AI) models with trillions ($10^{12}$) of parameters [1] is a paramount computational challenge that can only be tackled by massively parallel processing in ultra-scale AI clusters [2]. These computing clusters crucially rely on optical communication interfaces that leverage low-complexity intensity-modulation and direct-detection (IM/DD) schemes and that offer radically improved performance, efficiency and scalability as compared to current solutions. This poses stringent requirements on the underlying electro-optic (EO) modulators, especially with respect to modulation bandwidth, optical loss, $\pi$-voltage-length product $U_\pi L$, and resulting device footprint. Over the previous years, different modulator platforms have been explored, and their strengths and weaknesses have been identified in transmission experiments. The silicon photonic (SiP) platform stands out due to its intrinsic scalability and maturity, offering a wide portfolio of ready-to-use devices [3] that can be fabricated via well-established CMOS foundry processes [4], [5]. For all-silicon Mach-Zehnder

© 2026 IEEE. Personal use of this material is permitted. Permission from IEEE must be obtained for all other uses, in any current or future media, including reprinting/republishing this material for advertising or promotional purposes, creating new collective works, for resale or redistribution to servers or lists, or reuse of any copyrighted component of this work in other works.

modulators (MZM), the highest IM/DD line rate demonstrated so far amounts to 375 Gbit/s, achieved by six-level pulse-amplitude modulation (PAM6) [6] at a symbol rate of 145 GBd. However, the associated device is 1.5 mm long and features a large $\pi$-voltage $U_\pi$ in excess of 10 V, requiring a rather high drive voltage with a 5.4 $V_{pp}$ peak-to-peak swing [6]. Higher performance was achieved with indium phosphide (InP) MZMs, for which net data rates up to 400 Gbit/s have been demonstrated using 162 GBd probabilistically shaped (PS) PAM16 transmission [7], [8]. However, InP devices still feature comparatively high $\pi$-voltage length products $U_\pi L$ in excess of 5 Vmm and are subject to rather complex and costly fabrication processes on small-area substrates. Thin-film lithium niobate (TFLN) [9], [10] and thin-film lithium tantalate (TFLT) [11], [12] devices represent an attractive alternative, using crystalline Pockels material with utmost linearity. TFLN MZM have been demonstrated to allow 224 GBd PS-PAM14 signaling with net data rates of 633 Gbit/s [9]. However, device lengths are typically of the order of 1 cm, dictated by the rather high $U_\pi L$ product in excess of 14 Vmm [10], which impedes integration into small form-factor packages. As another ferroelectric material, barium titanate (BTO) has been intensively investigated over the previous years, and MZMs with $U_\pi L$ products down to 4.8 Vmm have been demonstrated and used for PS-PAM8 transmission at 122 GBd with net data rates of 300 Gbit/s [13]. However, the associated drive voltages of 3.7 $V_{pp}$ are still comparatively high. When it comes to modulation bandwidth, combining organic electro-optic (OEO) materials with plasmonic waveguide structures in so-called plasmonic-organic hybrid (POH) devices [14], [15] is an attractive concept, offering 3 dB bandwidths of hundreds of GHz [16], [17] along with $U_\pi L$ products of, e.g., 0.04 Vmm [18]. POH devices have been shown to support PS-PAM8 symbol rates of up to 160 GBd with net data rates of 419 Gbit/s [19]. However, plasmonic structures suffer from inherent optical losses of typically more than 400 dB/mm, which limits the device length to a few micrometers and results in rather high $\pi$-voltages of typically more than 7 V [19]. Hence, despite the various experimental demonstrations on different platforms, there is still an unmet need for a technology that can combine high modulation efficiency and large bandwidth with compact footprint and low optical loss, while ideally being amenable to cost-efficient mass production and monolithic co-integration with established SiP circuitry.

In this paper, we demonstrate a silicon-organic hybrid (SOH) MZM that has been specifically designed for high-speed IM/DD transmission by exploiting an advanced multi-level doping scheme [20], [21]. The SOH concept combines intrinsically scalable SiP waveguides with OEO cladding materials that are optimized on a molecular level for highest modulation efficiency and low optical loss [22], [23], [24]. Notably, SOH devices can be seamlessly co-integrated with the wealth of existing SiP devices without changing any front-end-of-line (FEOL) processes, thereby offering a direct path to cost-efficient mass production. Expanding on our previous results [21], our experiments rely on an SOH MZM with a $U_\pi L$ product of only 0.67 Vmm and highly compact 280 µm-long phase-shifter (PS) sections with sub-1 dB on-chip loss. The 3-dB bandwidth amounts to 74 GHz, and the 6-dB bandwidth exceeds our measurement range of 110 GHz. We demonstrate PAM4, PAM6, and PAM8 IM/DD signaling, reaching symbol rates of 204 GBd, 180 GBd, and 176 GBd, respectively, mainly limited by the bandwidth of our driver electronics and the receiver photodiode. For PAM8, we achieve line rates of 528 Gbit/s and net data rates of 410 Gbit/s, which, to the best of our knowledge, correspond to record-high values for MZM on the SiP platform. We believe that our results mark an important step towards cost- and power-efficient IM/DD transceivers for massively parallel AI clusters.

## II. SOH Integration: Augmenting the Silicon Photonics Platform

The concept of a silicon-organic hybrid (SOH) Mach-Zehnder modulator (MZM) is illustrated in Fig. 1. Fig. 1(a) shows a simplified schematic of an SOH MZM, indicating optical waveguides as solid black lines and a coplanar radio-frequency (RF) transmission line for the modulating signal in yellow. Note that the RF pads and tapers of the RF transmission line and the RF transmission line associated with the phase shifter are in different metal layers, as implied by the two color shades. Metal vias (not shown) are used to connect the different metal layers. Optical coupling to and from the chip is achieved either via grating couplers (GC) or edge couplers (EC), both connected to single-mode access strip waveguides on the chip. A 2×2 multi-mode interference (MMI) coupler is used to equally split the incoming light into the two MZM arms, each containing a strip-to-slot converter (S2Sl) that couples the light from a regular strip to the slot waveguide in the SOH phase modulator (PM) section. After the SOH PM, which feature a length 280 µm in our case, light is coupled back to strip waveguides using slot-to-strip converters (Sl2S) and then routed to a second MMI coupler that recombines both paths. The modulated light is then coupled out to a fiber via an EC or GC. Fig. 1(b) shows a cross-sectional view of a single SOH slot-waveguide PM along the line A – A' shown in Fig. 1(a). The optical slot waveguide is formed by two parallel silicon rails, separated by a narrow gap that is filled with a highly efficient organic electro-optic (OEO) material. Typical widths of the slots are in the range of 100 nm to 200 nm, and the rails are typically 200 nm to 260 nm wide, see [22] and [23] for further information on the SOH concept and the underlying design considerations. The rails are weakly $n$-doped and connected to thin adjacent $n$-, and $n^+$-doped silicon slabs [20]. The electrical modulation signal is applied via the co-planar RF transmission line consisting of three aluminum strips (Al, conductivity $3.7\times10^7$ S/m [25]) in ground-signal-ground (GSG) configuration. The strips are separated by an approximately 15 µm-wide gap which contains the 5 µm-wide oxide opening in the top oxide (TOX), which is filled with the organic electro-optic (OEO) material. Metal vias and highly doped silicon regions ($n^{++}$) connect the metal strips of the RF transmission line with the doped silicon slabs. Inset (1) of Fig. 1(b) shows an equivalent-circuit model of the slot waveguide cross section, where the resistances $R_{sb}$ of the doped slabs and rails and the slot capacitance $C_{sl}$ form a low-pass filter that could limit the modulation bandwidth – in addition to frequency

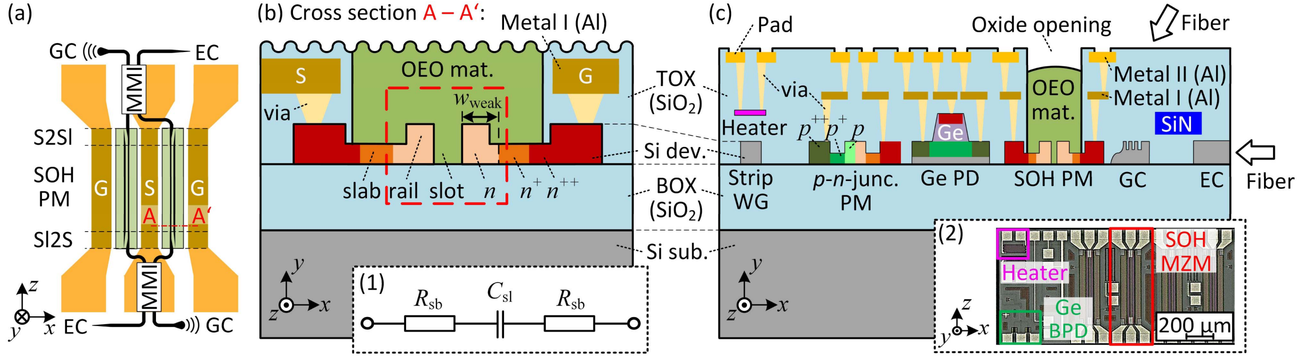


Fig. 1. Schematic and cross section of the high-speed SOH MZM. (a) Schematic top view of a single SOH MZM. The drive voltage is applied through a coplanar RF transmission line in ground-signal-ground (GSG) configuration. Light is coupled in and out of the MZM chip through grating couplers (GC) or edge couplers (EC). The on-chip light is split into two paths by a 2×2 multi-mode interference (MMI) coupler. Strip-to-slot (S2Sl) and slot-to-strip (Sl2S) converters couple light between strip-waveguide sections and the slot-waveguide sections of the SOH phase modulator (SOH PM). (b) Cross section of an SOH PM along the line A – A' in Subfigure (a). The optical slot waveguide is formed by two parallel weakly *n*-doped silicon rails that are separated by a slot filled with the OEO material (OEO mat., green). The rails are connected to the RF transmission line through aluminum vias and *n*-doped silicon slabs. Inset (1): Equivalent electrical circuit that can be used to represent a short element of the MZM transmission line [20], where the slab resistances $R_{sb}$ and the slot capacitance $C_{sl}$ form an RC lowpass. For increasing the RC bandwidth while keeping the optical loss low, multi-level doping with three levels ($n$, $n^+$, and $n^{++}$) is used [20]. The parameter $w_{weak}$ corresponds to the overall width of the weakly doped silicon region ($n$). (c) Cross section of the SOH PM, co-integrated with other standard devices of widely used silicon photonic (SiP) platforms. The wafer features a silicon substrate (Si sub.), a buried oxide ($SiO_2$ BOX, thickness: 3 µm) as well as a silicon device (Si dev.) layer and a protective top oxide (TOX) cover. For electrical connections, typically two or more metal layers (Metal I and II , Al) and associated vias are embedded into the TOX. From left to right, the following devices are depicted: A thermo-optical PS consisting of a silicon strip waveguide and an associated heater, a *p*-*n*-junction PM with the three donor ($n$, $n^+$ and $n^{++}$) and three acceptor ($p$, $p^+$ and $p^{++}$) doping levels, a germanium-based photodiode (Ge PD), and finally an SOH PM, for which the slot waveguide has been made accessible by a local opening in the TOX for depositing the OEO material. GC and EC are used for coupling of light between chip and external fibers. In some SiP platforms, an additional silicon nitride (SiN) layer is available within the TOX, e.g., for routing of high-power signals or for avoiding waveguide crossings in the SiP layer (Figure adapted from [3]) Inset (2): Top-view micrograph of a SiP chip fabricated by a commercial foundry, containing four SOH MZMs that are seamlessly co-integrated with other SiP devices such as thermal PS and balanced Ge PD (BPD).

dependent RF propagation loss [20]. A multi-level doping scheme is applied to the rails, the adjacent slabs, and the contact areas to maximize the bandwidth while keeping optical losses low [20]: Within the slot waveguide and in the directly adjacent regions of the slabs, the donor doping concentration ($n$) is low to minimize free-carrier absorption (FCA), while the doping increases ($n^+$) further away from the waveguide for maximum bandwidth before it reaches a highly degenerate contact doping level ($n^{++}$) at the ohmic transition to the metal vias. The $n$-doped region features a resistivity in the range from $5.5\times10^{-4}$ Ωm to $49.5\times10^{-4}$ Ωm [20] and a width of $w_{weak} = 340$ nm, while the resistivity of the $n^+$-doped region is in the range of $1\times10^{-4}$ Ωm to $4\times10^{-4}$ Ωm [20]. To guarantee ohmic contact between the doped silicon and the metal electrodes, the contact level doping $n^{++}$ is highly degenerate, and the resistivity of the associated areas can be neglected.

Notably, the basic structure of the SOH MZM as depicted in Fig. 1(a) and (b) is fully compatible with standard front-end-of-line (FEOL) fabrication processes in SiP foundries, while the OEO materials can be applied in back-end-of-line (BEOL) post-processing steps, which are described in more detail below. These steps do not interfere with the rather complex and highly sensitive FEOL SiP foundry processes, allowing to combine SOH device with the rich portfolio of proven silicon photonic devices that have been developed over the previous years [3], [6], [26], [27], [28]. This is illustrated in Fig. 1(c), showing the schematic cross-section of an SOH phase modulator (SOH PM) side-by-side with the cross sections of other widely used SiP devices that are offered as standard components of SiP process design kits (PDK). These components comprise, e.g., SiP strip waveguides (Strip WG), rib waveguides (not shown), often complemented by additional silicon-nitride (SiN) waveguide layers within the TOX [29]. When combined with heaters, Si strip waveguides can act as phase-shifters, that are slow, but offer low optical loss [30]. Faster phase modulators (PM) have to rely on *p*-*i*-*n*- or *p*-*n*-junctions that are integrated into the optical waveguide (*p*-*n*-junc. PM), while detection of signals can make use of germanium photodiodes (Ge PD) [3], both involving different levels of donor ($n$, $n^+$, $n^{++}$) and acceptor ($p$, $p^+$, $p^{++}$) doping as indicated by red and green colors, respectively. Electrical connections rely on different layers of metal lines (Metal 1, Metal 2) in the TOX, which are linked through associated vias and which can be contacted through pads on the chip surface. Coupling of light to and from external fibers can rely on GC or EC, possibly in combination with advanced coupling schemes such as photonic wire bonds [31], [32], [33]. SOH PM can rely on the same basic waveguide structures, doping techniques, and electrical interconnect layers as conventional SiP devices and only require a local oxide opening for BEOL deposition of the OEO material. Such oxide openings are routinely used in silicon photonic biosensors [34], [35], and are frequently offered as additional features of standard MPW processes [3], [36], [37]. Monolithic co-integration of proven SiP devices with highly efficient SOH PM leads to a versatile and powerful platform that combines the inherent scalability of advanced CMOS fabrication processes with the performance and flexibility of optimized OEO materials. Inset (2) of Fig. 1(c) shows a top-view micrograph of one of the resulting SiP chips, comprising four SOH MZM that are seamlessly integrated with Ge-based balanced PD (BPD, green) as well as thermal PS (magenta) based on heaters.

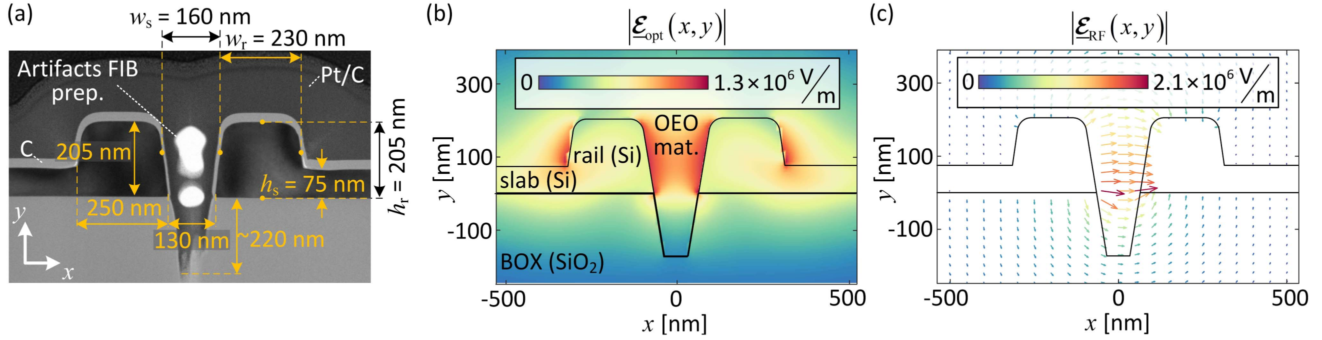


Fig. 2. Cross-sectional analysis and numerical simulations of the SOH slot waveguide. (a) Bright-field transmission-electron microscope (TEM) image of the slot waveguide within the region as marked by the red dashed frame in Fig. 1(b). We find that the local removal of the TOX leads to an approximately 220 nm-deep trench that is etched into the BOX layer under the slot. The Si rails feature a sidewall angle of 10° with respect to the normal to the wafer surface along with rounded corners, having a radius of approximately 40 nm. The height of the Si rails and the thickness of the adjacent Si slabs amounts to 205 nm and 75 nm, which is 15 nm less than the targeted values of $h_r = 220$ nm and $h_s = 90$ nm, respectively. The average slot width measured at half the rail height amounts to the designed $w_s = 160$ nm, and the measured rail width of approximately 230 nm is only slightly below the targeted $w_r = 240$ nm. The white patches in the slot region are an artifact from sample preparation and can be disregarded. (b) Magnitude $|\mathcal{E}_{opt}(x,y)|$ of electric field associated with the optical quasi-TE mode as obtained from a numerical simulation (CST Microwave Studio, Dassault Systèmes, Paris, France) of the slot waveguide filled with the OEO material (OEO mat.). The field strengths correspond to a modal power of 1 mW. As expected for a slot waveguide, the optical mode is concentrated in the slot region. (c) Representation of the transverse electric-field vectors $|\mathcal{E}_{RF}(x,y)|$ associated with the modulating radio-frequency (RF) mode field at an exemplary modulation frequency of 1 GHz. The color indicates again the magnitude of the field for an overall modal power of 1 mW.

The BEOL post-processing of SOH devices comprises several steps for deposition, poling, and encapsulation of the OEO material, which are described in more detail in the following. Our current devices rely on SOXD-100 (SilOriX GmbH, Karlsruhe, Germany) as an OEO material, which is provided in solid form and which needs to be dissolved in an appropriate solvent such as 11,2-trichloroethane prior to deposition. A thin glass canula with an opening diameter of a few tens of micrometers, which is attached to an $(x,y,z)$-positioner, is then dipped into the solution and filled via capillary forces. Once filled, the glass canula is gently brought into contact with the chip surface such that a meniscus with a diameter of a few tens of micrometers forms. The canula is then slightly lifted up while maintaining the meniscus and moved laterally across the chip surface to draw a line of OEO material solution along the oxide opening with the exposed slot waveguides. Note that all the critical dimensions of the SOH slot-waveguide device are defined by the front-end-of-line (FEOL) processes of the SiP foundry and that OEO material deposition can hence rely on rather simple and fast processes that do not need to guarantee precise layer thicknesses. The canula-based dispensing technique described here is only one option – alternatively, ink-jet printing can be used, which holds the potential to reduce cycle time for OEO material deposition to 1 s or less [38]. After deposition of the material, the OEO chromophores within the slot waveguide are randomly oriented, and an acentric order has to be imposed in a one-time poling process to achieve macroscopic electro-optic activity, see [22] and [23] for details. To this end, a DC poling voltage is applied to the floating ground (G) electrodes of the MZM, resulting in poling directions of the two arms that allow for efficient push-pull operation of the device and hence for efficient chirp-free amplitude modulation [22]. In a final step, the OEO material is encapsulated to prevent in-diffusion of oxygen, thereby avoiding optically induced degradation of the device at high intensities [39], [40].

It should be noted that, for a long time, long-term stability has been one of the major concerns when it comes to practical application of SOH devices. However, similar to the evolution of organic light-emitting devices (OLEDs) approximately two decades ago [41], there has recently been significant progress in device architectures, material concepts, and processing techniques, showing a path to overcome these challenges [40], [42]. More specifically, there are two types of degradation mechanisms related to the OEO material in SOH devices: De-poling of the materials by re-orientation of the OEO chromophores under high temperatures, as well as photochemical degradation of the underlying functional groups under high optical intensities [39]. Regarding de-poling at high temperatures, one solution is to increase the glass-transition temperature $T_g$ of the OEO material [18], [43], [44], [45], [46], [47], which can, e.g., be accomplished by attaching bulky adamantyl side groups to the chromophores [43], [44] and/or by choosing appropriate material matrices [45], [46]. These approaches have been shown to offer glass-transition temperatures of, e.g., 182 °C, permitting stable device operation at temperatures as high as 110 °C [43], which are sufficient for many applications. An alternative approach relies on cross-linking of OEO materials upon poling, making use of appropriate chemical side groups [18], [47]. This leads to a rigid 3D lattice in the OEO material, significantly increasing the glass-transition temperature to beyond 170 °C [18], which permits operation and storage temperatures of, e.g., 120 °C and beyond [47] – sufficient even for communication applications with advanced requirements [48]. With respect to photochemical degradation under high intensities, proper encapsulation of the OEO material is key. More specifically, just like in OLEDs, high intensities can lead to photo-oxidation [39], which can be avoided by protecting the OEO materials from oxygen in-diffusion using properly designed barrier layers [40], [42]. With this approach, up to 2000 hours of photostability without degradation of the

$\pi$-voltage could be demonstrated for an SOH MZM that was operated with intensities of more than 5 MW/cm$^2$ in the OEO material – orders of magnitude higher than the intensities at the surface of the sun [40]. Note that, to keep the technical effort manageable, our proof-of-concept devices demonstrated here did not yet use cross-linking or hermetic encapsulation of the OEO materials, but should be amenable to such techniques while maintaining their outstanding performance advantages.

## III. Characterization and Analysis of the Fabricated SOH MZM

The function of the SOH PM and the associated MZM crucially relies on the shape and the exact dimensions of the underlying slot waveguide [22], [23], which often have to be chosen according to the capabilities and limitations of the underlying fabrication processes. One of the most crucial parameters is the slot width $w_\mathrm{s}$, which has a major impact on the $\pi$-voltage-length product $U_\pi L$ of the device. This can be intuitively understood by considering the fact that the sidewalls of the silicon rails effectively act as electrodes for the applied RF field. Hence, for a given applied voltage, the modulating electric field strength in the slot is inversely proportional to the slot width $w_\mathrm{s}$, thereby decreasing the $U_\pi L$-product in proportion to $w_\mathrm{s}$, see (1) below. However, there are technological and material-related limitations in reducing the slot width too much. On the technology side, the minimal slot width is often dictated by the resolution of the underlying structuring processes of the foundry, which depends both on the lithography tools and the etching processes. Moreover, the behavior of the organic electro-optic (OEO) material in the slot plays an important role. More specifically, in narrower slots, a larger fraction of chromophore molecules is subject to interactions with the side-walls, inhibiting the re-orientation of chromophores during the poling process [22], [23], [49]. A slot width of 160 nm was found to offer a good compromise between low $U_\pi L$-products on the one hand and manufacturing yield and poling efficiency on the other hand. Based on the slot width of $w_\mathrm{s} = 160$ nm, an intermediate rail width of $w_\mathrm{r} = 240$ nm was found to maximize the interaction factor between the optical and RF mode, while the height of $h_\mathrm{r} = 220$ nm of the rail is usually dictated by the standard device-layer thickness of the underlying silicon-on-insulator (SOI) wafers. The choice of the slab height $h_\mathrm{s} = 90$ nm is also the result of a trade-off between low optical losses in the slot waveguide and small $U_\pi$ on the one hand and the EO modulation bandwidth on the other hand. More specifically, for a fixed doping concentration, the sheet resistance of the slab increases if the slab height is reduced. Hence, the corner frequency of the associated RC circuit, see Inset 1 of Fig. 1(a), reduces and the RF attenuation due to ohmic losses increases, resulting in a smaller modulation bandwidth. Moreover, for larger values of $h_\mathrm{s}$, a larger fraction of the optical mode propagates in the doped silicon slabs. This leads to higher optical losses due to free-carrier absorption (FCA) and to a reduced interaction factor of the optical mode with the OEO material in the slot. Within the regime of available choices offered in standard foundry processes, a slab height of 90 nm offers the best compromise.

Clearly, the slot waveguide of a manufactured SOH MZM will not perfectly match the idealized schematic in Fig. 1(b) since the device is subject to unavoidable fabrication tolerances. To investigate this aspect and to consider them in our design, we investigated the exact cross-sectional geometry of our devices by transmission-electron microscopy (TEM), see Fig. 2(a). The bright-field TEM image represents the cross section of a slot waveguide as marked by the red dashed box in Fig. 1(b). The image was taken from a raw device that did not have an OEO layer yet, and a carbon (C) and a platinum carbon (Pt/C) layer were deposited to increase the conductivity of the sample for high-quality TEM imaging and to protect it during preparation by focused ion-beam milling (FIB). The white patches in the slot waveguide are an artifact from sample preparation and can be disregarded. From the TEM image, we extract a silicon rail height of 205 nm (targeted height: 220 nm) and width of 250 nm, measured at the interface between the Si device and the BOX layer (targeted width: 240 nm). The Si slab is 75 nm high (targeted height: 90 nm), and the slot is 130 nm wide at the interface between the Si device and the BOX layer, while the average width amounts to roughly 160 nm (targeted width $w_\mathrm{s} = 160$ nm). Compared to the ideal design, the sidewalls of the Si rails are not vertical, but feature a sidewall angle of approximately 10°. Furthermore, the corners of the rails are rounded with a radius of approximately 40 nm. The fabricated devices also exhibit approximately 220 nm-deep trenches etched through the slot into the BOX layer during local removal of the TOX on top of the slot waveguides. The trench is comparatively rough at the bottom. Note, however, that this roughness is still reasonably far away from the optical mode field, see Fig. 2(b), such that we do not expect any significant contribution to optical scattering losses. Based on the slot-waveguide geometry extracted from the TEM image, we conducted further optical and RF mode-field simulations. Fig. 2(b) shows the normalized magnitude of the optical mode field $|\underline{\varepsilon}_\mathrm{opt}(x,y)|$ in the $x$-$y$-plane as obtained from a numerical simulation using CST microwave studio (Dassault Systèmes, Paris, France), and Fig. 2(c) shows the associated transverse RF field vectors $|\underline{\varepsilon}_\mathrm{RF,t}(x,y)|$ for a frequency of 1 GHz. For the RF simulation, we assumed dielectric constants of $\varepsilon_\mathrm{r,Si} = 11.9$, $\varepsilon_\mathrm{r,SiO2} = 3.75$, and $\varepsilon_\mathrm{r,OEO} = 3.2$ for silicon, $SiO_2$, and the OEO material, respectively. Both the optical as well as the RF field are well confined to the slot waveguide.

With these field distributions at hand, we can quantify the interaction of the optical field and the RF field for the actually fabricated devices. To this end, we calculate the so-called field-interaction factor $\Gamma$, which, for a push-pull device operated at low frequencies, is related to the low-frequency $\pi$-voltage-length product $U_\pi L$ via [50], [51]

$$U_\pi L = \frac{1}{2} \frac{\lambda w_\mathrm{s}}{n_\mathrm{OEO}^3 r_{33,\mathrm{OEO}} \Gamma}. \tag{1}$$

In this relation, $\lambda$ refers to the optical wavelength in vacuum, $w_\mathrm{s}$ is the slot width, and $n_\mathrm{OEO}$ and $r_{33,\mathrm{OEO}}$ are the refractive index and the Pockels coefficient of the OEO material, respectively. At low frequencies, far below the cut-off frequency of the *RC*-type low-pass associated with the slot capacitance and the resistance of the adjacent silicon rails and slabs, see Inset (1) of

Fig. 1(b), the field-interaction factor $\Gamma$ is real-valued and given by [50], [51]

$$\Gamma = \frac{1}{2}\frac{n_{\mathrm{OEO}}w_{\mathrm{s}}}{Z_0\mathcal{P}_{\mathrm{opt}}\mathcal{U}} \times \iint_{A_{\mathrm{OEO}}} \left|\underline{\boldsymbol{\mathcal{E}}}_{\mathrm{opt}}(x,y)\right|^2 \left|\underline{\boldsymbol{\mathcal{E}}}_{\mathrm{RF}}(x,y)\right| \cos^2(\vartheta_{\mathrm{opt}}(x,y))dx\,dy. \tag{2}$$

In this relation, $Z_0 = 377\,\Omega$ is the free-space wave impedance, $\mathcal{P}_{\mathrm{opt}}$ is the power associated with the optical eigenmode field $\underline{\boldsymbol{\mathcal{E}}}_{\mathrm{opt}}(x,y)$, and $\mathcal{U}$ corresponds to the amplitude of the voltage that is associated with the eigenmode field $\underline{\boldsymbol{\mathcal{E}}}_{\mathrm{RF}}(x,y)$, like the one shown in Fig. 2(c). For non-zero modulation frequencies, $\mathcal{U}$ can be obtained from the power $\mathcal{P}_{\mathrm{RF}}$ of the RF eigenmode field and from the real part $\Re\{\underline{Z}_{\mathrm{L}}\} \approx 49.2\ \Omega$ of the corresponding line impedance $\underline{Z}_{\mathrm{L}}$ associated via the relation $\mathcal{U} = \sqrt{2\mathcal{P}_{\mathrm{RF}}\,\Re\{\underline{Z}_{\mathrm{L}}\}}$. The angle $\vartheta_{\mathrm{opt}}(x,y)$ denotes the local angle between the electrical field $\underline{\boldsymbol{\mathcal{E}}}_{\mathrm{opt}}(x,y)$ of the optical mode and the chromophore orientation as imposed by a poling field [51]. From the fields simulated for the real structure as shown in Fig. 2 above, we obtain a field-interaction factor $\Gamma_{\mathrm{real}} \approx 0.185$, assuming a slot width of $w_{\mathrm{s}} = 160$ nm. Note that this value is even slightly higher than the field-interaction factor $\Gamma_{\mathrm{ideal}} = 0.154$ that is obtained from the idealized, targeted structure as shown in Fig. 1(b). We attribute this to the fact that the slabs of the real structure are lower compared to the idealized structure, resulting in smaller fraction of the optical mode propagating in the slab and a stronger confinement to the slot region. To confirm our hypothesis, we repeat the simulation for the targeted idealized structure, but with a reduced slab height of 75 nm and a rail height of 205 nm, which would lead to an interaction factor of 0.19 – slightly higher than the interaction factor $\Gamma_{\mathrm{real}}$ calculated for the real waveguide geometry. The efficiency of the SOH PM hence clearly depends on the underlying geometry, thus supporting the importance of measuring and taking into account real rather than idealized device structures.

With the real field-interaction factor $\Gamma_{\mathrm{real}}$ according to (2) at hand, we can translate the measured $U_\pi L$-product of our devices into the associated Pockels coefficient $r_{33,\mathrm{OEO}}$. After deposition and poling of the highly efficient OEO chromophore, we measure a $U_\pi$ of 2.4 V, corresponding to a $U_\pi L$ of 0.67 Vmm given the 280 µm long slot-waveguide sections of our device. Using (1) along with the field-interaction factor $\Gamma_{\mathrm{real}} = 0.185$ for the real device, we calculate an in-device EO coefficient $r_{33,\mathrm{OEO}}$ of 158 pm/V.

Another important figure of merit for EO modulators, that strongly depends on the fabrication of the device, is the optical loss. Fig. 3(a) shows the on-chip optical transmission spectrum of the SOH MZM after the BEOL processing. This measurement was taken through the grating couplers (GC) illustrated in Fig. 1(a), and the GC influence was removed by measuring an associated reference structure on the same chip. Note that the strip waveguides in the MZM arms feature a length difference of 40 µm, see Fig. 1(a). The resulting arm-length imbalance leads to fringes in the transmission spectrum having a period of approximately 1.5 THz (12 nm). We can use these fringes to extract the insertion loss (IL) and the extinction ratio (ER) directly from the optical transmission spectrum of the MZM, which is routinely taken as part of wafer-level test procedures. In contrast to that, for an MZM with balanced arm lengths, a DC voltage needs to be applied and swept to extract the IL and the ER. This requires separate electrical probes, complicating wafer-level characterization of the devices. As a side effect of the imbalanced arm lengths, the operation point of the MZM can simply be adjusted via wavelength-tuning of the carrier. The measured extinction ratio (ER) of the device used in our experiments is 38 dB at 1550 nm, and the on-chip insertion loss (IL) amounts to 2.7 dB at a center wavelength $\lambda = 1550$ nm, for which all components such as the MMI couplers as well as the SI2S a S2SI converters were designed.

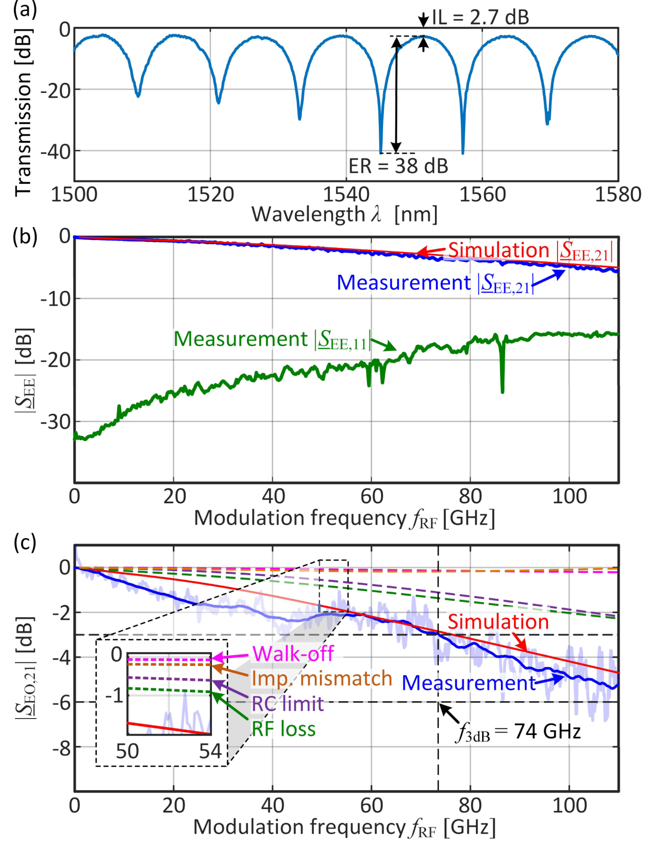


Fig. 3. Optical transmission spectrum and bandwidth measurement of the SOH MZM. (a) On-chip optical transmission spectrum of the SOH MZM, having an insertion loss (IL) of 2.7 dB and an extinction ratio (ER) of 38 dB around the targeted wavelength of 1550 nm. Note that the arm lengths of the MZM differ by 40 µm, which leads to frequency-dependent fringes in the transmission spectrum having a period of approximately 1.5 THz (12 nm). We can use these fringes to extract the insertion loss (IL) and the extinction ratio (ER) directly from the optical transmission spectrum of the MZM. (b) Measured (blue) and simulated (red) electric (EE) transmission $|\underline{S}_{21}|$ and reflection $|\underline{S}_{11}|$ (green) as a function of modulation frequency $f_{\mathrm{RF}}$. (c) Magnitude of the measured (blue) and simulated (red) electro-optic (EO) transfer function $|\underline{S}_{21}|$ normalized to its magnitude at $f_{\mathrm{RF}} = 70$ kHz as a function of modulation frequency $f_{\mathrm{RF}}$. The contributions of different simulated bandwidth-limiting effects are shown in the same graph, see Appendix A for details on the underlying mathematical model. We find that the impact of walk-off (magenta) between RF and optical mode and of impedance mismatch (Imp. mismatch, brown) is negligible. The *RC* lowpass filter (purple) and RF loss (green) contribute roughly equally.

TABLE I
OPTICAL LOSSES OF THE VARIOUS BUILDING BLOCKS OF THE SOH MZM. THE TOTAL ON-CHIP LOSS OF THE CURRENT DEVICE GENERATION AMOUNTS TO 2.7 dB WITH THE SLOT-WAVEGUIDE PS FILLED WITH OEO MATERIAL CONTRIBUTING 0.9 dB. WITH FURTHER OPTIMIZATION OF THE VARIOUS COMPONENTS, ON-CHIP INSERTION LOSSES BELOW 2 dB SHOULD BE WITHIN REACH.

| **Component** | **Loss per length/ device** | **Total loss** |
|---|---|---|
| MMI coupler | 0.2 dB per device | 0.4 dB |
| S2Sl / Sl2S | 0.4 dB per device | 0.8 dB |
| Strip waveguide | 0.2 dB/mm | 0.6 dB |
| Slot-waveguide PS | 3.2 dB/mm | 0.9 dB |
| **Total** | - | 2.7 dB |

To identify the loss contributions of the individual MZM components, we measured dedicated test structures on the same wafer, featuring cascades of MMI couplers and S2Sl/Sl2S converter, see Table I for a summary of the results. For the two 2×2 MMI couplers, we find an excess loss of 0.2 dB per device, contributing 0.4 dB to the overall MZM insertion loss. For the S2Sl and Sl2S converters, the loss amounts to 0.4 dB per device, contributing another 0.8 dB to the total on-chip loss. The 2×2 MMI couplers of our devices are fully covered by TOX ($SiO_2$, refractive index $n_{\mathrm{SiO2}} = 1.44$ at $\lambda = 1.55$ µm), whereas the strip-to-slot converters are covered by the OEO material (refractive index $n_{\mathrm{OEO}} = 1.8$ at $\lambda = 1.55$ µm). The transition from the TOX cladding to the OEO material is hence located in the strip waveguide, where the impact is much lower than in the slot waveguide. Our test-structure cascades for the S2Sl and Sl2S converters feature the same design, such that the measured losses of these structures already account for the losses of the cladding-material transitions. For the strip waveguides, we measure a set of cutback test structures, leading to loss of 0.2 dB/mm, close to the value specified by the foundry. With a total length of 3 mm for the access strip waveguide, on-chip routing hence contributes 0.6 dB of losses. Starting from the measured overall on-chip MZM loss of 2.7 dB and taking into account the aforementioned losses of the various components, we find a remaining loss of 0.9 dB that can be assigned to the slot-waveguide phase shifter, see Table I. This value is on par with previously reported sub-1 dB phase-shifter losses of high-speed SOH MZM [24]. The length-related propagation loss of the phase shifter amounts to 3.2 dB/mm – slightly higher than previously reported values of, e.g., 2.5 dB/mm [24]. This increase is attributed to the rather high doping of the silicon rails and the adjacent slab regions, that was chosen to achieve a high bandwidth [20]. Still, the insertion loss of the phase-shifter sections is significantly smaller than those offered by other high-speed silicon photonic modulators [3], [6]. To the best of our knowledge, our device corresponds to the first MZM on the silicon photonic platform reaching line rates of more than 200 Gbit/s while maintaining a sub-1 dB phase-shifter loss.

Note that the losses listed in Table I can be further reduced. More specifically, optimized geometries of MMI couplers can lower the excess loss to values of less than 0.1 dB per MMI coupler [52]. For the S2Sl and Sl2S converters, losses of 0.1 dB or even below have been previously demonstrated, even tough for slightly different slot geometries [24], [33], [53]. Finally, the losses in the slot waveguide can be further reduced by either optimizing the etching processes leading to lower sidewall roughness or further optimizing the doping schemes. With all these proposed steps, on-chip losses well below 2 dB are within reach.

To assess the high-speed behavior of the device, we measure the electrical scattering parameters of the GSG RF transmission line and the associated slot-waveguide phase modulator sections using a vector network analyzer (VNA, Anritsu MS4647B with 3743 A mmWave extender modules). To measure only the scattering parameters of our device while excluding the RF probes, the extender modules and the associated RF cables, we perform a short-open-load-through (SOLT) calibration using a 50 Ω calibration substrate (MPI AC-2), thereby effectively moving the measurement plane of the VNA to the tips of the RF probe. We then contact the input and the output pads of the GSG transmission line and measure the transmission $|\underline{S}_{\mathrm{EE},21}|$ (blue) as well as of the reflection $|\underline{S}_{\mathrm{EE},11}|$ (green), see blue and green traces in Fig. 3(b). The 320 µm-long RF transmission line of our device is fairly well matched to 50 Ω, with the reflection being below −20 dB up to a frequency of 65 GHz, and below −15 dB up to 110 GHz, while the transmission drops to −5.5 dB at 110 GHz. We compare the transmission measurement to the results of a simulation (CST Microwave Studio, Dassault Systèmes, Paris, France), indicated by a red trace in Fig. 3(b). In this simulation, we reproduce the device geometry as shown in Fig. 2 with the exact slot-waveguide geometry and the associated conductivities and further include the finite resistivity and the associated RF losses of the underlying Si handle wafer. We find that the measured and simulated transmission $|\underline{S}_{\mathrm{EE},21}|$ are in good agreement. From our simulation, we furthermore confirm that most of the RF losses are caused by ohmic losses in the low-doped silicon regions, labelled by "$n$ doping" in Fig. 1(b). The RF losses could thus be reduced by omitting the low doping, effectively treating the now undoped silicon as a dielectric. This approach effectively trades an increased $U_\pi$ for a higher modulation bandwidth [54]. Alternatively, the slabs can be replaced entirely with a high-k dielectric [50], [51], resulting in capacitive coupling between the RF transmission line and the slot waveguide. Note, however, that this approach is currently not compatible with the FEOL of SiP foundries.

In a next step, we measure the electro-optic (EO) transfer characteristics of our device. To this end, we again drive the MZM via the first port of the VNA while feeding it with an optical carrier tuned to the quadrature point. The modulated optical output signal is then received by a calibrated 110 GHz photodiode (Anritsu MN4765B-0072) that is connected to the second port of the VNA, while the detached RF probe is now used to terminate the device with a 50 Ω impedance. To isolate the EO transfer function of the MZM, we use a different calibration strategy which accounts for the characteristics of the remaining RF probe and the associated cables that are still used to drive the device as well as for the PD. The isolated electro-optic (EO) transfer function $|\underline{S}_{\mathrm{EO},21}|$ of the MZM is then normalized to its magnitude at 70 kHz. The result is indicated by blue traces

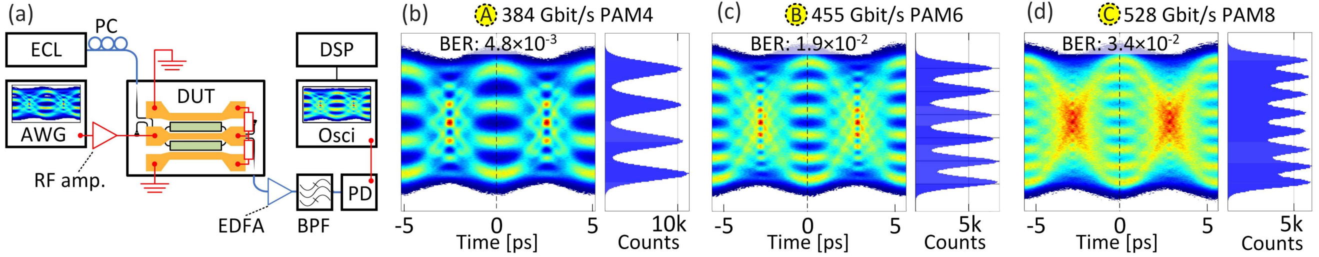


Fig. 4. Experimental demonstration of high-speed data transmission (a) Experimental setup: Light from an external-cavity laser (ECL) is sent through a polarization controller (PC) and coupled to the device under test (DUT) via an edge coupler (EC). An arbitrary-waveform generator (AWG) provides the electrical drive signal, which is boosted by an RF amplifier (RF amp.). After the DUT, the optical signal is sent through an erbium-doped fiber amplifier (EDFA), which is needed only to reach the rather high power levels required by the high-speed PD used in our experiments. The EDFA is followed by a bandpass filter (BPF) and a variable optical attenuator (VOA, not shown). The PD output is directly recorded by a real-time oscilloscope (RTO). Offline digital-signal-processing (DSP) is used to recover the signal and to calculate the bit error ratio (BER). (b)–(d) Selected recorded eye patterns, bit error ratios (BER), and histograms for PAM4 (384 Gbit/s line rate, 192 GBd symbol rate), PAM6 (455 Gbit/s line rate, 176 GBd symbol rate) and PAM8 (528 Gbit/s line rate, 176 GBd symbol rate). To the best our knowledge, the line rate of 528 Gbit/s achieved for 176 GBd PAM8 transmission corresponds to the highest value so far achieved for an MZM on the silicon photonics platform. The BER, achievable information rate (AIR), and net data rate for the depicted eye diagrams are indicated as data points by Ⓐ, Ⓑ, and Ⓒ in Fig. 5.

in Fig. 3(c), where the light blue line corresponds to the raw data while the blue line is a smoothed version, obtained by calculating the moving-average of the raw data over a bandwidth of 10 GHz. Using the averaged transfer function, we find a 3 dB EO bandwidth of 74 GHz, and a 6 dB EO bandwidth beyond 110 GHz, as indicated by the black dashed lines at −3 dB and −6 dB in Fig. 3(c).

To verify our analytical model and to gain further insight into different bandwidth-limiting effects and their contribution to the EO frequency response, we compare our measured transfer function to results of a simulation, see red trace in Fig. 3(c). The simulation is based on an optoelectronic model of our device that is similar to the approach described in [20] but uses a more sophisticated approach for quantifying the frequency-dependent interaction between the optical and the RF mode, see Appendix A for more details. The simulation results are in fair agreement with the measurements, see red and blue traces in Fig. 3(c). Notably, our model allows to study different bandwidth-limiting effects separately, as indicated by the dashed magenta, brown, purple, and green traces in Fig. 3(c). As already suggested by the rather low measured back-reflection $|\underline{S}_{\mathrm{EE},11}|$ in Fig. 3(b), the impact of impedance mismatch (Imp. mismatch, brown) is negligible. Moreover, since our device is fairly short, the walk-off between optical and RF mode (magenta) has also only a minor impact. In contrast to that, the RF loss of the transmission line (green) as well as the bandwidth limit of the $RC$ low-pass formed by the slot capacitance $C_{\mathrm{sl}}$ and the slab resistance $R_{\mathrm{sb}}$ (purple), see Inset (1) in Fig. 1(b), contribute roughly equally, with RF loss even slightly dominating. This observation is again in good agreement with the measured EE transfer function shown in Fig. 3(b). Note that, in the refined model presented in Appendix A, the behavior of the $RC$ low-pass is represented by introducing a frequency-dependent $\pi$-voltage-length product $\underline{\Pi}_{\mathrm{MZM}}$, see Appendix A for details. Notably, the 3 dB-bandwidth of the $RC$ low-pass is beyond our 110 GHz measurement range, meaning that a SOH MZM with even higher bandwidth can be implemented by simply shortening the length of the device – possibly in combination with more efficient OEO materials that counteract the associated increase of the $\pi$-voltage $U_\pi$.

## IV. Data Transmission Experiment

To demonstrate the functional performance our MZM, we conduct a high-speed data communication experiment, see Fig. 4(a) for the underlying setup. An external-cavity laser (ECL) with 13 dBm of output power provides the optical carrier at a wavelength of 1556 nm. The carrier is coupled to the device under test (DUT) via a lensed fiber and an EC. The electrical drive signal is generated by an arbitrary-waveform generator (AWG, Keysight M8199B, 6 dB-bandwidth of 80 GHz) and sent through a 20 cm-long RF cable to an RF amplifier (RF amp., SHF T850B) that is directly connected to 110 GHz probe (MPI Titan T110A). A linear minimum-mean-square-error (MMSE) predistortion is applied during drive-signal synthesis to compensate for the RF losses in the cable and for the roll-off of both the AWG and the RF amplifier. The MZM transmission line is terminated with a second probe and an attached 50 Ω resistor. In the fiber after the DUT, we measure an optical power of 1.7 dBm, which is compliant with typical specifications for high-speed optical Ethernet transceivers [55]. Note that the optical output power of the transmitter could be increased even further by reducing the fiber-to-chip coupling losses of currently ∼3 dB per interface to values of, e.g., 1.3 dB, that are routinely reached by photonic wire bonding of single-mode fibers to edge-coupled silicon photonic waveguides [32]. Still, an additional erbium-doped fiber amplifier (EDFA) was needed in the experiment to reach a sufficient power level of 10 dBm for the 90 GHz high-speed PD at the receiver (Finisar BPDV4120R). Note that a real-world transceiver implementation could rely on a sufficiently broadband RF amplifier after the PD, thereby rendering the EDFA unnecessary. Out-of-band noise from the EDFA is suppressed by a tunable bandpass filter (BPF), and a variable optical attenuator (VOA, not shown) allows to set the power at the PD input. The output waveform of the PD is sampled by a 256 GSa/s real-time oscilloscope (RTO, Keysight UXR1104A) and then sent through an offline digital signal processing (DSP) chain, which contains up-sampling, timing recovery, linear Sato-equalization [56], and decision-directed least-mean-square equalization.

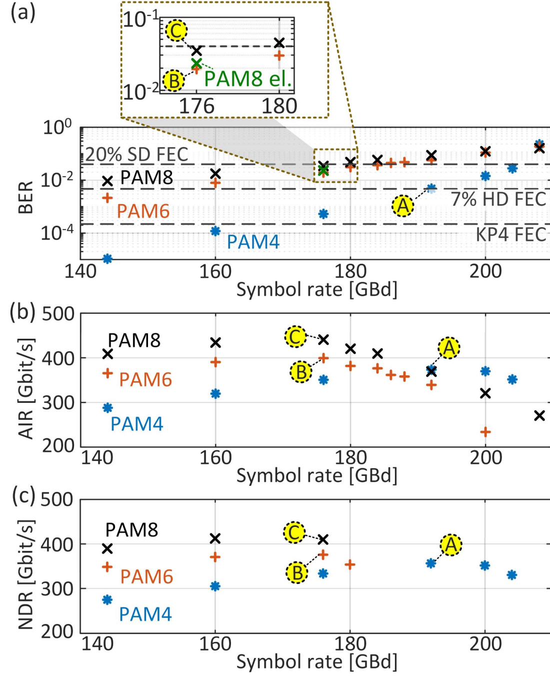


Fig. 5. Bit error ratio (BER), achievable information rate (AIR), and net data rate (NDR) vs. symbol rate for PAM4 (✳), PAM6 (+) and PAM8 (✕). The data points labeled Ⓐ, Ⓑ, and Ⓒ correspond to the eye patterns shown in Fig. 4(b) – (d). (a) BER as a function of symbol rate. The dark grey dashed lines indicate the BER thresholds for soft-decision (SD) forward error correction (FEC) with 20% overhead (20% SD FEC), for hard-decision (HD) FEC with 7% overhead (7% HD FEC), and for KP4 FEC. As a benchmark, we also measured the PAM8 BER in the electrical back-to-back (elec. B2B) case (✕), see zoom-in. This measurement shows that most of the signal distortions are already present in the MZM drive signal. For 176 GBd PAM8, 180 GBd PAM6, and 204 GBd PAM4 transmission, the BER is still below the SD FEC threshold with 20% overhead. To the best of our knowledge, for each modulation format, these symbol rates are the highest so far demonstrated for an MZM on the SiP platform. (b) AIR vs. symbol rate: For each BER, the NGMI is calculated and then used as a base for obtaining the theoretically achievable information rate (AIR). (c) Taking the overhead of real FEC implementations into account [59], we obtain the achievable net data rate (NDR) for the various symbol rates. We reach a net data rate of 412.5 Gbit/s for 160 GBd PAM8 signaling, which is also a record value for MZM on the silicon platform.

In our experiments, we tested three different modulation formats, PAM4, PAM6 and PAM8. For each modulation format, an exemplary received eye diagram together with the corresponding bit error ratio (BER) is depicted in Fig. 4(b)–(d). To the right of each eye diagram, the histogram recorded in the center (time $t = 0$; marked by black, dashed vertical line) is depicted. For PAM4 with a line rate of 384 Gbit/s (symbol rate 192 Gbd), four levels can be clearly distinguished at a BER of $4.8\times10^{-3}$. For PAM6 at a line rate of 455 Gbit/s (symbol rate 176 GBd), the six levels are still well discernable in the histogram at a BER of $1.9\times10^{-2}$. For PAM8 at a line rate of 528 Gbit/s (symbol rate 176 GBd), our communication system starts to reach its limits and the eight levels start to strongly overlap. The associated BER of $3.4 \times 10^{-2}$, however, is still below the threshold for soft-decision forward error correction (SD-FEC) with a 20 % overhead [57]. In Fig. 5(a), the BER as a function of the symbol rate is shown for PAM4 (✳), PAM6 (+) and PAM8 (✕), along with the thresholds for SD-FEC with 20% overhead, for hard-decision (HD) FEC with 7% overhead, and for KP4-FEC with 5.84% overhead. For PAM4, PAM6 and PAM8, the highest symbol rates with BER below the 20% SD-FEC limit amount to 204 GBd (line rate 408 Gbit/s), 184 GBd (line rate 476 Gbit/s) and 176 GBd (line rate 528 Gbit/s), respectively. For PAM4, we measure a BER below the 7% HD-FEC limit up to 176 GBd (line rate 352 Gbit/s). For each of these modulation formats, we achieve the highest symbol rates so far demonstrated with an MZM on the SiP platform. For each measurement, the normalized general mutual information (NGMI) is calculated based on a log-likelihood ratio assuming additive white Gaussian noise as the main channel impairment [58]. Using the NGMI, the achievable information rate (AIR) is calculated and depicted in Fig. 5(b).

We also calculate the net data rate (NDR) in accordance with FEC implementations reported in [59], see Fig. 5(c). In all graphs of Fig. 5, the data points associated with the eye diagrams shown in Fig. 4(b)–(d) are labeled Ⓐ, Ⓑ, and Ⓒ. With PAM4, the highest NDR amounts 356.5 Gbit/s, achieved with a symbol rate of 192 GBd. For PAM6, we record a NDR of up to 375.9 Gbit/s at a symbol rate of 176 GBd. For the highest line rate of 528 Gbit/s, obtained for 176 GBd PAM8 signaling, we obtain an NDR of 410 Gbit/s. With PAM8 at 160 GBd (line rate 480 Gbit/s), the NDR is even slightly higher at 412.5 Gbit/s, corresponding to the highest value so far demonstrated for MZM on the SiP platform. Note that the signal quality at high symbol rates is strongly impaired by our AWG and RF cables, which have a significant roll-off at frequencies beyond 80 GHz. To test the minimum achievable BER of our electrical system, we directly connect the output of the RF amplifier to the input of the RTO, to measure the electrical back-to-back performance. For PAM8 and a symbol rate of 176 GBd, we obtain a BER of $2.2\times10^{-2}$ for the electrical B2B (PAM8 el.), see green cross (✕) in Fig. 5(a), which is only slightly below the BER of $3.4\times10^{-2}$ that we measured for the optical communication setup containing our SOH MZM. At symbol rates approaching 200 GBd, the bandwidth of our PD further limits the performance of our system. Hence, we believe that with signal generators and photodiodes having a larger bandwidth, a NDR approaching 500 Gbit/s could be achieved with our device.

We finally benchmark the performance of our SOH device against other state-of-the-art MZMs based on different technology platforms, see Table II. Our comparison starts from the current SOH device in the first row of Table II ("This work") and comprises other SOH devices [60], depletion-based silicon photonic (SiP) MZMs [6], [61], thin-film lithium niobate (TFLN) [9], [62], [63] and thin-film lithium tantalate (TFLT) [11] MZMs, barium titanate (BTO) devices [13], as well as indium phosphide (InP) [7], [8] and plasmonic-organic hybrid (POH) [17], [19] MZMs. Column 2 of Table II provides the $\pi$-voltage $U_\pi$, Columns 3 and 4 the optical loss and the length of the phase-shifter section of the different devices. Note that for some devices [6], [13], [62], [63], the phase-shifter losses were not explicitly stated and had to be estimated from the overall MZM losses. In these cases, which are marked by a star ($*$) in Column 3, we assumed an excess loss of the underlying power splitters and combiners of 0.25 dB each – a rather high value, which leads to a rather optimistic estimate

TABLE II

COMPARISON OF THE SOH MZM PRESENTED HERE (“THIS WORK”) WITH OTHER HIGH-SPEED MACH-ZEHNDER MODULATOR (MZM) TECHNOLOGIES AND ASSOCIATED HIGH-SPEED SIGNALING EXPERIMENTS. COLUMNS 2, 3, 4, AND 5 PROVIDE THE $\pi$-VOLTAGES $U_\pi$, THE OPTICAL LOSS AND THE LENGTH OF THE PHASE SHIFTER, AND THE 3 DB MODULATION BANDWIDTH, RESPECTIVELY. COLUMN 6 QUANTIFIES THE AMENABILITY OF THE RESPECTIVE MODULATOR TECHNOLOGY TO CO-INTEGRATION WITH ESTABLISHED SIP CIRCUITRY – THE MAINSTAY PLATFORM FOR OPTICAL TRANSCEIVERS RANKING FROM RATHER LIMITED CO-INTEGRATION POTENTIAL WITH A RATING OF 1 TO READILY AVAILABLE COMMERCIAL OFFERINGS WITH A RATING OF 4. COLUMNS 7 AND 8 FINALLY SPECIFY THE SYMBOL RATES AND MODULATION FORMATS AS WELL AS THE RESULTING LINE RATES THAT HAVE BEEN ACHIEVED IN RECENT TRANSMISSION EXPERIMENTS. SOH DEVICES STAND OUT BY OFFERING A UNIQUE COMBINATION OF LOW OPTICAL LOSS, LOW $\pi$-VOLTAGE, HIGH LINE RATE, AND COMPACT FOOTPRINT WITH FULL AMENABILITY TO MONOLITHIC CO-INTEGRATION WITH STANDARD SIP CIRCUITS. WE HENCE BELIEVE THAT THE TECHNOLOGY IS WELL POSITIONED FOR FUTURE GENERATIONS OF HIGH-SPEED OPTICAL TRANSCEIVERS.

| Tech. | $U_\pi$ | Phase-shifter loss | Phase-shifter length | 3dB BW | SiP comp. | IM/DD symbol rate (mod. Format) | Line rate | Ref. |
|---|---|---|---|---|---|---|---|---|
| SOH | 2.4 V | 0.9 dB | 280 µm | 74 GHz | 3 | 176 GBd (PAM8)<br>204 GBd (PAM4) | 528 Gbit/s<br>408 Gbit/s | This work |
| | 0.9 V | 2 dB | 500 µm | - | 3 | 192 GBd (PAM4) | 384 Gbit/s | [60] |
| SiP | 10 V | 3.1 dB* | 1 mm | 42 GHz | 4 | 145 GBd (PAM6) | 375 Gbit/s | [6] |
| | 5.1 V | 9.9 dB | 3.7 mm | 43 GHz | 4 | 182 GBd (OOK)<br>154 GBd (PAM4) | 182 Gbit/s<br>308 Gbit/s | [61] |
| TFLN | - | - | - | - | 1 | 224 GBd (PS-PAM14) | 798 Gbit/s | [9] |
| | 1 V | 1.8 dB* | 24 mm | 110 GHz | 1 | >200 GBd (PAM8)** | > 600 Gbit/s** | [62] |
| | 1.3 V | 0.7 dB* | 20 mm | > 50 GHz | 1 | - | - | [63] |
| TFLT | 4.8 V | 0.2 dB | 6 mm | 110 GHz | 1 | 176 GBd (PAM8)<br>208 GBd (OOK) | 528 Gbit/s<br>208 Gbit/s | [11] |
| BTO | 3.2 V | 1.5 dB* | 1.5 mm | - | 2 | 110 GBd (PAM8)<br>128 GBd (PAM4) | 330 Gbit/s<br>254 Gbit/s | [13] |
| InP | 1.5 V | 1 dB* | 3.6 mm | 80 GHz | 2 | 162 GBd (PS-PAM16) | 517 Gbit/s | [7],[8] |
| POH | 12 V | 5.6 dB | 10 µm | 997 GHz | 2 | 176 GBd (PAM8) | - | [17] |
| | 7.3 V | 5.3 dB | 12.5 µm | 100 GHz | 2 | 256 GBd (OOK) | 528 Gbit/s<br>256 Gbit/s | [19] |

* Phase-shifter losses estimated from MZM losses.

** IM/DD line rate estimated based from performance obtained in the coherent transmission experiment.

for the phase-shifter loss. Column 5 provides the 3 dB EO modulation bandwidth, and Column 6 quantifies the amenability of the respective modulator technology to co-integration with established SiP circuitry – the mainstay platform for optical transceivers. This aspect is an important aspect for cost-efficient mass production. We quantify the SiP compatibility on a scale from 1 to 4, where 4 represents the highest level of compatibility and is assigned to conventional SiP modulators. If a device is part of the silicon device layer itself but needs additional back-end-of-line (BEOL) fabrication steps, as is the case for SOH devices, we assign a rating of 3. InP, BTO, and POH MZM can be integrated on the SiP platform, e.g., by heterogeneous approaches [64], [65], but require changes of the front-end-of-line (FEOL) fabrication processes, which is costly and comes with additional complexity. We hence assign a rating of 2 to these devices. For TFLN and TFLT, typical MZM devices lengths are of the order of 5 mm or more – a significant size mismatch compared to rather compact SiP devices. We hence believe that co-integration of TFLT and TFLN with silicon photonic circuitry will not reach a level of compactness and scalability that is comparable to that of other devices, and we assign a rating of 1 to those concepts. Columns 7 and 8 finally provide the symbol rates and modulation formats as well as the resulting line rates that have been achieved in recent transmission experiments. Note that in some experiments, the top-performing TFLN MZM [62] were only demonstrated as part of an in-phase/quadrature (IQ) modulator. In this case, the achievable IM/DD line rate was estimated based on the performance obtained in the coherent transmission experiment.

Compared to other technologies, only the SOH, InP, TFLT and TFLN platform can simultaneously offer low phase-shifter losses (1 dB or less) and low $\pi$-voltages $U_\pi$ [7], [8], [11], [60], [62], [63], [64]. However, TFLN and TFLT MZM require large footprints to achieve low $\pi$-voltages, thereby limiting the integration density, which might limit their usability in co-packaged optical transceivers that support many parallel lanes. Furthermore, the compatibility of TFLN, TLFT with SiP is relatively poor. In case of InP devices, the $\pi$-voltage-length product $U_\pi L$ is still relatively high, typically in excess of 5 Vmm, often resulting in rather long devices [7], [8], which are additionally subject to rather complex and costly fabrication processes on small-area substrates. POH MZM, on the other hand, are highly compact and hence offer utmost integration density [17], [19], but suffer from high optical losses. This limits the device length to a few micrometers, resulting in relatively high $\pi$-voltages [19] – aside from the fact that co-integration of plasmonic devices with SiP circuits remains challenging. Hence, we believe the SOH platform, combining high efficiency, low loss, and high bandwidth with full amenability to monolithic co-integration with standard SiP circuits is well positioned for future generations of high-speed optical transceivers.

## V. SUMMARY

We demonstrate a 280 µm-long silicon-organic hybrid (SOH) Mach-Zehnder modulator (MZM), seamlessly co-integrated with standard silicon photonic circuitry obtained through foundry-based fabrication processes. Relying on a multi-level doping scheme, the modulator combines a $U_\pi L$ product of

0.67 Vmm and sub-1 dB phase-shifter losses with an electro-optic (EO) 3 dB bandwidth of 74 GHz and a 6 dB bandwidth beyond 110 GHz. We demonstrate signaling at 204 GBd PAM4 (line rate 408 Gbit/s), 180 GBd PAM6 (line rate 465 Gbit/s), and 176 GBd PAM8 (line rate 528 Gbit/s), all with a BER below the threshold of soft-decision forward error correction (SD-FEC) with a 20 % coding overhead. To the best of our knowledge, this corresponds to the highest symbol rates and line rates for all these modulation formats for MZM on the silicon photonic platform. We reach a net data rate of 412.5 Gbit/s for 160 GBd PAM8 signaling, which is also a record value for MZM on the silicon platform. While the symbol rates and signal quality of our current experiments is mainly limited by the drive electronics and the bandwidth of the receiver photodiode, the performance of the SOH MZM can be further improved, e.g., by refining the device design to increase the bandwidth. We therefore believe that our results mark an important step towards compact and efficient IM/DD transceivers based on the silicon photonics platform, that offer net data rates of 400 Gbit/s per channel or more.

## APPENDIX

For the numerical simulation of the EO bandwidth of our SOH MZM, see Fig. 3 and the associated discussion in Section III above, we developed a novel model to precisely quantify the frequency-dependent interaction between the optical and the RF mode within the SOH slot waveguide. In contrast to the model described in [20], our scheme does not rely on an equivalent-circuit approach to quantify the *RC* low-pass effects of the slot-waveguide structure, see Inset 1 of Fig. 1(b), and does hence not require any additional approximations for the slot capacitance and the slab resistances. Instead, we use numerical simulations of the full optical and electrical RF mode fields and analyze their interaction through a vectorial coupled-mode approach. This leads to a frequency-dependent complex-valued $\pi$-voltage-length product $\underline{\Pi}_{\mathrm{PM}} = \underline{U}_{\pi,\mathrm{PM}}L$, that can be interpreted as a generalization of the low-frequency real-valued $U_{\pi,\mathrm{PM}}L$ that is specified in (1) above and which only applies to modulation frequencies far below the *RC* cut-off frequency. In the following, we explain our approach step by step, starting from the schematic of an SOH phase modulator (PM) comprising a single slot waveguide along with a ground-signal-type RF transmission line, see Fig. 6(a). The device is driven by a signal source, characterized by its source impedance $\underline{Z}_{\mathrm{S}}$, which may in general be complex-valued, and an open-circuit voltage $u_{\mathrm{S}}(\mathrm{t}) = \Re\{\underline{U}_{\mathrm{S}}\exp(\mathrm{j}2\pi f_{\mathrm{RF}}t)\}$, where $f_{\mathrm{RF}}$ denotes the RF modulation frequency. Note that the open-source voltage amplitude $\underline{U}_{\mathrm{S}}$ of the signal source corresponds to twice the voltage amplitude $\underline{U}_{\mathrm{m}}$ that would be effective at the input of a perfectly matched load with impedance $\underline{Z}_{\mathrm{S}}^{*}$, i.e., $\underline{U}_{\mathrm{S}} = 2\,\underline{U}_{\mathrm{m}}$. The transmission line of length $L$ features a generally complex-valued frequency-dependent characteristic impedance $\underline{Z}_{\mathrm{L}}$ and is terminated by a generally complex-valued termination impedance $\underline{Z}_{\mathrm{T}}$. We neglect any impact of back-reflected RF power on the signal source and express the voltage emitted from the source towards the SOH PM as a power wave $U_{\mathrm{RF,in}}^{(+)}(t) = Re\{\underline{U}_{\mathrm{RF,in}}^{(+)}e^{\mathrm{j}2\pi f_{\mathrm{RF}}t}\}$,

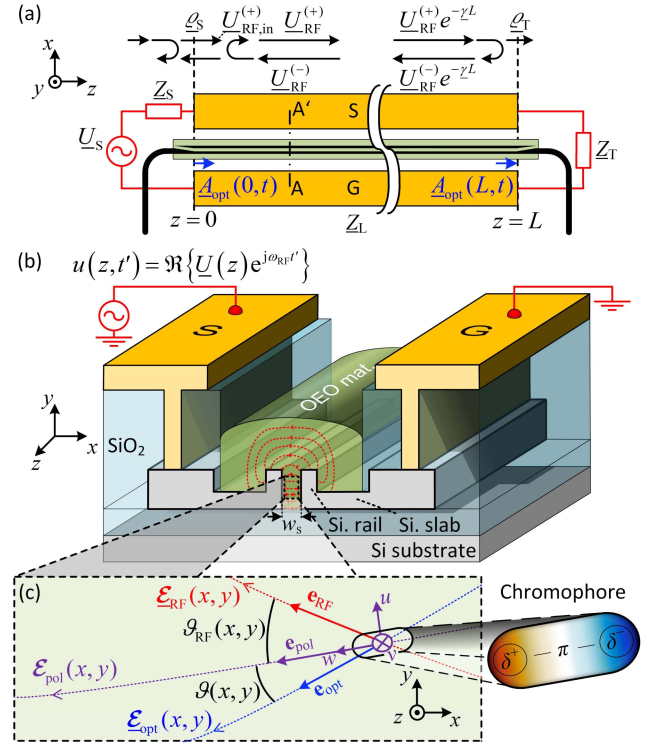


Fig. 6. Illustration of electrical and optical models of an SOH phase modulator (PM). (a) Electrical model: An RF voltage source (internal impedance $\underline{Z}_{\mathrm{S}}$) providing an internal drive voltage $u_{\mathrm{S}}(\mathrm{t}) = \Re\{\underline{U}_{\mathrm{S}}\exp(\mathrm{j}2\pi f_{\mathrm{RF}}t)\}$, is connected to the transmission line of the SOH PM, which has a length $L$ and a line impedance $\underline{Z}_{\mathrm{L}}$ and which is terminated by an impedance $\underline{Z}_{\mathrm{T}}$. In general, the impedances are not perfectly matched, and the RF signal is reflected at $z = 0$ and $z = L$ with reflection coefficients $\underline{\varrho}_{\mathrm{S}}$ and $\underline{\varrho}_{\mathrm{T}}$, respectively. This leads to a partially standing wave with amplitude $\underline{U}(z)$, formed by the superposition of forward and backward propagating voltage waves. These waves are quantified by their complex-valued amplitudes $\underline{U}_{\mathrm{RF}}^{(+)}$ and $\underline{U}_{\mathrm{RF}}^{(-)}$ at $z = 0$, while $U_{\mathrm{RF,in}}^{(+)}$ refers to the portion of the source voltage wave that passes through the interface at z=0 and is actually coupled to the transmission line. The optical signal, represented by a complex-valued amplitude $\underline{A}_{\mathrm{opt}}(z,t)$, accumulates a phase $\varphi(t)$ between $z = 0$ and $z = L$ as a consequence of its EO interaction with the RF signal on the transmission line. (b) Optical model: Cross section of the SOH PM along A–A' as illustrated in Subfigure (a). The layer stack is similar to Fig. 1(b). The OEO material is indicated in green. (c) Definition of poling direction and field directions: The poling direction $\mathbf{e}_{\mathrm{pol}}$ refers to the average local orientation of the chromophores and is assumed ot correspond to the poling field $\boldsymbol{\mathcal{E}}_{\mathrm{pol}}(x,y)$ (purple dashed lines) applied during the initial poling step. The $w$-axis of the local coordinate system ($u$, $v$, $w$) is choosen along the poling direction $\mathbf{e}_{\mathrm{pol}}$, while $v$ is oriented along the waveguide axis and $u$ is within the transverse plane. The directions $\mathbf{e}_{\mathrm{opt}}$ and $\mathbf{e}_{\mathrm{RF}}$ of the electrical fields $\boldsymbol{\mathcal{E}}_{\mathrm{opt}}(x,y)$ and $\boldsymbol{\mathcal{E}}_{\mathrm{RF}}(x,y)$ associated with the optical mode and the RF mode are shown in blue and red, respectively. We define the angles $\vartheta_{\mathrm{opt}}(x,y)$ between the optical and poling field and $\vartheta_{\mathrm{RF}}(x,y)$ between the RF and poling field.

where the complex-valued voltage $\underline{U}_{\mathrm{RF,in}}^{(+)}$ is given by

$$\underline{U}_{\mathrm{RF,in}}^{(+)} = \underline{U}_{\mathrm{S}}\frac{\underline{Z}_{\mathrm{L}}}{\underline{Z}_{\mathrm{S}}+\underline{Z}_{\mathrm{L}}}. \tag{3}$$

In these relations, the superscript '(+)' indicates that the associated voltage wave propagates in forward direction, i.e., along the positive $z$-direction, whereas a superscript '(-)' is used for a backward-propagating wave. For a perfectly matched load, half of the RF power is dissipated in the internal impedance $\underline{Z}_{\mathrm{S}}$, and the other half is coupled to the device. If there is, in addition,

an impedance mismatch between the line impedance $\underline{Z}_{\mathrm{L}}$ and the internal source impedance $\underline{Z}_{\mathrm{S}}$, only a part of the non-dissipated half of the RF power is coupled to the PM transmission line, while the remainder is reflected back into the source. These effects are already contained in (3). If there is additionally a mismatch between the termination impedance $\underline{Z}_{\mathrm{T}}$ and the line impedance $\underline{Z}_{\mathrm{L}}$, the RF signal wave is reflected back and forth between the input ($z = 0$) and the output ($z = L$) of the MZM transmission line, resulting in partially standing wave, see Fig. 6(a). The complex-valued voltages of the forward-, and backward-propagating partial waves can be expressed as $\underline{U}_{\mathrm{RF}}^{(+)} e^{-\underline{\gamma} z}$ and $\underline{U}_{\mathrm{RF}}^{(-)} e^{\underline{\gamma} z}$, respectively, where $\underline{U}_{\mathrm{RF}}^{(+)}$ and $\underline{U}_{\mathrm{RF}}^{(-)}$ correspond to the wave amplitudes at $z = 0$, i.e., at the beginning of the transmission line. The complex-valued RF propagation parameter $\underline{\gamma}$ is given by

$$\underline{\gamma} = \alpha_{\mathrm{RF}} + j\frac{2\pi f_{\mathrm{RF}}}{v_{\mathrm{p,RF}}} = \alpha_{\mathrm{RF}} + j\frac{2\pi f_{\mathrm{RF}}}{c} n_{\mathrm{e,RF}}, \tag{4}$$

with $v_{\mathrm{p,RF}} = c/n_{\mathrm{e,RF}}$ being the phase velocity of the RF wave and $n_{\mathrm{e,RF}}$ representing the effective index of the underlying RF mode, while $\alpha_{\mathrm{RF}}$ is the RF amplitude attenuation coefficient, corresponding to a power attenuation coefficient of $2\alpha_{\mathrm{RF}}$. The reflections at both ends of the RF transmission line are quantified by the complex-valued amplitude reflection factors $\underline{\varrho}_{\mathrm{S}}$ and $\underline{\varrho}_{\mathrm{T}}$,

$$\underline{\varrho}_{\mathrm{S}} = \frac{\underline{Z}_{\mathrm{S}} - \underline{Z}_{\mathrm{L}}}{\underline{Z}_{\mathrm{S}} + \underline{Z}_{\mathrm{L}}}, \tag{5}$$

$$\underline{\varrho}_{\mathrm{T}} = \frac{\underline{Z}_{\mathrm{T}} - \underline{Z}_{\mathrm{L}}}{\underline{Z}_{\mathrm{T}} + \underline{Z}_{\mathrm{L}}}, \tag{6}$$

which couple the forward- and the backward-propagating signal at both ends of the transmission line.

With the complex voltages wave amplitudes $\underline{U}_{\mathrm{RF}}^{(+)}$ and $\underline{U}_{\mathrm{RF}}^{(-)}$ of the forward- and backward-propagating RF signals at hand, we can express the complex-valued vectorial electric field $\underline{\mathbf{E}}_{\mathrm{RF}}(x, y, z)$ at any point of the SOH PM via the forward- and backward-propagating modal fields $\underline{\boldsymbol{\mathcal{E}}}_{\mathrm{RF}}^{(+)}$ as well as $\underline{\boldsymbol{\mathcal{E}}}_{\mathrm{RF}}^{(-)}$, respectively,

$$\underline{\mathbf{E}}_{\mathrm{RF}}(x, y, z) = \frac{\underline{U}_{\mathrm{RF}}^{(+)}}{\underline{\mathcal{U}}^{(+)}} e^{-\underline{\gamma} z} \underline{\boldsymbol{\mathcal{E}}}_{\mathrm{RF}}^{(+)}(x, y) + \frac{\underline{U}_{\mathrm{RF}}^{(-)}}{\underline{\mathcal{U}}^{(+)}} e^{\underline{\gamma} z} \underline{\boldsymbol{\mathcal{E}}}_{\mathrm{RF}}^{(-)}(x, y). \tag{7}$$

In these relations, the quantities $\underline{\mathcal{U}}^{(+)}$and $\underline{\mathcal{U}}^{(-)}$ denote the complex-valued voltage amplitudes that are associated with the forward- and backward-propagating mode fields, $\underline{\boldsymbol{\mathcal{E}}}_{\mathrm{RF}}^{(+)}$ and $\underline{\boldsymbol{\mathcal{E}}}_{\mathrm{RF}}^{(-)}$, respectively. By proper normalization of the mode fields and by proper choice of their phases, $\underline{\mathcal{U}}^{(+)}$and $\underline{\mathcal{U}}^{(-)}$ can be made real-valued and equal

$$\mathcal{U} = \underline{\mathcal{U}}^{(+)} = \underline{\mathcal{U}}^{(-)} \tag{8}$$

In the following, we make the simplifying assumption that the electrical fields $\underline{\boldsymbol{\mathcal{E}}}_{\mathrm{RF}}^{(+)}(x, y)$ and $\underline{\boldsymbol{\mathcal{E}}}_{\mathrm{RF}}^{(-)}(x, y)$ associated with the RF wave correspond to quasi-TEM modes that can be reasonably well approximated by their transverse components $\underline{\mathcal{E}}_{\mathrm{RF},x}^{(+)}(x, y)$ and $\underline{\mathcal{E}}_{\mathrm{RF},y}^{(+)}(x, y)$ as well as $\underline{\mathcal{E}}_{\mathrm{RF},x}^{(-)}(x, y)$, and $\underline{\mathcal{E}}_{\mathrm{RF},y}^{(-)}(x, y)$, respectively. Note that the relative phase of these components does not depend on the propagation direction such that we can represent the forward- and the backward-propagating mode field by the same expression

$$\underline{\boldsymbol{\mathcal{E}}}_{\mathrm{RF}}^{(+)}(x, y) \approx \underline{\boldsymbol{\mathcal{E}}}_{\mathrm{RF}}^{(-)}(x, y) \approx \begin{pmatrix} \underline{\mathcal{E}}_{\mathrm{RF},x}(x, y) \\ \underline{\mathcal{E}}_{\mathrm{RF},y}(x, y) \\ 0 \end{pmatrix} = \underline{\boldsymbol{\mathcal{E}}}_{\mathrm{RF}}(x, y). \tag{9}$$

Equation (6) can then be written as

$$\underline{\mathbf{E}}_{\mathrm{RF}}(x, y, z) = \frac{\underline{\boldsymbol{\mathcal{E}}}_{\mathrm{RF}}(x, y)}{\mathcal{U}} \left( \underline{U}_{\mathrm{RF}}^{(+)} e^{-\underline{\gamma} z} + \underline{U}_{\mathrm{RF}}^{(-)} e^{\underline{\gamma} z} \right). \tag{10}$$

In a next step, we analyze the impact of the imperfect impedance matching at the source and the termination side. To this end, we relate the forward- and backward-propagating voltage waves at position $z = 0$ and $z = L$ as well as the drive signal $\underline{U}_{\mathrm{RF,in}}^{(+)}$ injected by the source at $z = 0$ via the respective reflection coefficients,

$$\underline{U}_{\mathrm{RF}}^{(-)} e^{\underline{\gamma} L} = \underline{\varrho}_{T} \underline{U}_{\mathrm{RF}}^{(+)} e^{-\underline{\gamma} L}, \tag{11}$$

$$\underline{U}_{\mathrm{RF}}^{(+)} = \underline{U}_{\mathrm{RF,in}}^{(+)} + \underline{\varrho}_{\mathrm{S}} \underline{U}_{\mathrm{RF}}^{(-)}. \tag{12}$$

With (10), (11), and (12), we can express $\underline{U}_{\mathrm{RF}}^{(+)}$ and $\underline{U}_{\mathrm{RF}}^{(-)}$ via the drive signal $\underline{U}_{\mathrm{RF,in}}^{(+)}$ and rewrite (7) as [60]

$$\underline{\mathbf{E}}_{\mathrm{RF}}(x, y, z) = \frac{\underline{\boldsymbol{\mathcal{E}}}_{\mathrm{RF}}(x, y)}{\mathcal{U}} \frac{\underline{U}_{\mathrm{d}} \underline{Z}_{\mathrm{L}}}{\underline{Z}_{\mathrm{S}} + \underline{Z}_{\mathrm{L}}} \frac{e^{-\underline{\gamma} z} + \underline{\varrho}_{\mathrm{T}} e^{\underline{\gamma} z} e^{-2\underline{\gamma} L}}{1 - \underline{\varrho}_{\mathrm{S}} \underline{\varrho}_{\mathrm{T}} e^{-2\underline{\gamma} L}}. \tag{13}$$

The real valued, time-dependent electric vector fields of the RF wave at any point of the PM is then given by

$$\mathbf{E}_{\mathrm{RF}}(x, y, z, t) = \Re\left\{ \underline{\mathbf{E}}_{\mathrm{RF}}(x, y, z)\, e^{j\omega_{\mathrm{RF}} t} \right\}. \tag{14}$$

For the optical signal, we express the electric and magnetic vectorial fields $\underline{\mathbf{E}}_{\mathrm{opt}}(x, y, z)$ and $\underline{\mathbf{H}}_{\mathrm{opt}}(x, y, z)$ within the slot waveguide phase modulator by the vectorial electric and magnetic mode fields $\underline{\boldsymbol{\mathcal{E}}}_{\mathrm{opt}}(x, y)$ and $\underline{\boldsymbol{\mathcal{H}}}_{\mathrm{opt}}(x, y)$ with an associated modal propagation constant $\beta$ and a complex-valued slowly varying envelope $\underline{A}_{\mathrm{opt}}(z, t)$, which propagates in the positive $z$-direction with a group velocity $v_{\mathrm{g}} = c/n_{\mathrm{eg,opt}}$, where $n_{\mathrm{eg,opt}}$ denotes the effective group refractive index of the optical mode. This leads to expressions of the form

$$\underline{\mathbf{E}}_{\mathrm{opt}}(x, y, z, t) = \underline{A}_{\mathrm{opt}}(z, t) \frac{\underline{\boldsymbol{\mathcal{E}}}_{\mathrm{opt}}(x, y)}{\sqrt{\mathcal{P}_{\mathrm{opt}}}} e^{j(\omega t - \beta z)}, \tag{15}$$

$$\underline{\mathbf{H}}_{\mathrm{opt}}(x, y, z, t) = \underline{A}_{\mathrm{opt}}(z, t) \frac{\underline{\boldsymbol{\mathcal{H}}}_{\mathrm{opt}}(x, y)}{\sqrt{\mathcal{P}_{\mathrm{opt}}}} e^{j(\omega t - \beta z)}, \tag{16}$$

where $\omega$ refers to the optical angular frequency $\omega = 2\pi c/\lambda$. Note that we assumed the SOH PM to have negligible optical back reflections such that we only need to consider forward-propagating modes $\underline{\boldsymbol{\mathcal{E}}}_{\mathrm{opt}}(x, y)$ and $\underline{\boldsymbol{\mathcal{H}}}_{\mathrm{opt}}(x, y)$. The modal power $\mathcal{P}_{\mathrm{opt}}$ associated with the mode fields $\underline{\boldsymbol{\mathcal{E}}}_{\mathrm{opt}}(x, y)$ and $\underline{\boldsymbol{\mathcal{H}}}_{\mathrm{opt}}(x, y)$ given by

$$\mathcal{P}_{\mathrm{opt}} = \frac{1}{2} \iint \Re\left\{ \underline{\boldsymbol{\mathcal{E}}}_{\mathrm{opt}}(x, y) \times \underline{\boldsymbol{\mathcal{H}}}_{\mathrm{opt}}^{*}(x, y) \right\} \mathbf{e}_{z} \mathrm{d}x\, \mathrm{d}y. \tag{17}$$

To relate a change of the RF field within the slot-waveguide structure to a phase change $\varphi$ of the optical mode, we investigate the evolution of the complex optical envelope $\underline{A}_{\mathrm{opt}}(z, t)$ during

propagation along $z$ in the active section of the SOH PM. To this end, we introduce a retarded time-frame with $t' = t - z/v_g$, within which the evolution of $\underline{A}'_{\text{opt}}(z, t')$ can be described by differential equation of the form [67]

$$\frac{\partial \underline{A}'_{\text{opt}}(z,t')}{\partial z} = -j\Delta\beta(z,t')\underline{A}'_{\text{opt}}(z,t'). \tag{18}$$

In this relation, $\Delta\beta(z, t')$ denotes the local change of the modal propagation constant $\beta$ due to the modulating RF field and $\underline{A}'_{\text{opt}}(z, t')$ refers to the slowly varying envelope as a function of the retarded time $t'$, as opposed to $\underline{A}_{\text{opt}}(z, t)$, which is defined with respect to the natural time $t$. Solving the differential equation in the interval $z \in [0, L]$ leads to

$$\underline{A}'_{\text{opt}}(z=L,t') = \underline{A}'_{\text{opt}}(0,t')e^{j\varphi_{\text{PM}}(t')}, \tag{19}$$

where the phase modulation $\varphi_{\text{PM}}$ is given by

$$\varphi_{\text{PM}}(t') = \int_0^L \Delta\beta(z,t')\,\mathrm{d}z. \tag{20}$$

Based on 1.68 in [67], $\Delta\beta(z, t')$ can be expressed via the voltage-induced anisotropic perturbation of the relative permittivity profile $\Delta\boldsymbol{\varepsilon}_{\text{r}}(x,y,z,t')$,

$$\Delta\beta\left(z,t'\right) = \frac{\omega}{4\mathcal{P}_{\text{opt}}}\iint\left[\varepsilon_0\Delta\boldsymbol{\varepsilon}_{\text{r}}\left(x,y,z,t'\right)\underline{\boldsymbol{\mathcal{E}}}_{\text{opt}}(x,y)\right]\underline{\boldsymbol{\mathcal{E}}}^*_{\text{opt}}(x,y)\mathrm{d}x\,\mathrm{d}y. \tag{21}$$

where $\varepsilon_0 = 8.854\times10^{-12}$ As/Vm is the vacuum permittivity. For a small perturbation, we can express $\Delta\boldsymbol{\varepsilon}_{\text{r}}$ by the change of the corresponding (3×3) impermeability tensor $\Delta\boldsymbol{\eta}$ [51],

$$\Delta\boldsymbol{\varepsilon}_{\text{r}}\left(x,y,z,t'\right) = -\boldsymbol{\varepsilon}_r\left(x,y,z\right)\Delta\boldsymbol{\eta}\left(x,y,z,t'\right)\boldsymbol{\varepsilon}_r\left(x,y,z\right). \tag{22}$$

The change of the impermeability tensor $\Delta\boldsymbol{\eta}$ is given by the product of the appropriate elements of the electro-optic tensor $\boldsymbol{r}$ with the corresponding components of the modulating RF wave. The underlying operations are most conveniently performed in a coordinate system ($u$, $v$, $w$), that is referred to the electro-optic material, see Fig. 6(c). The coordinate system ($u$, $v$, $w$) is chosen such that the $w$-axis is oriented along the average local direction of the elongated chromophores, in the direction of the resulting average dipole moment. The term "average" used here accounts for the fact that, even after poling, the orientation of the chromophores is still subject to a stochastic distribution such that we have to rely on the mean direction obtained when averaging over many chromophores in a volume element at the respective position. We assume that the average direction of the dipole moment is parallel to the local poling field that is generated when applying a DC poling voltage to the electrodes of the device during the initial poling step. Since this DC field does not have any longitudinal component, we can assume that the $w$-axis of our material coordinate system is entirely within a transverse ($x$, $y$)-plane, see Fig. 6(c). The $v$-direction is then chosen along the $z$-axis of the waveguide coordinate systems, while the $u$-direction is perpendicular to $v$ and $w$ and is selected to obtain a right-handed coordinate system ($u$, $v$, $w$). We assume further that the electro-optic effect is exclusively caused by the hyperpolarizability along the axis of the elongated chromophore, which, on average, is oriented along the local $w$-direction. The electro-optic interaction is hence fully quantified by the electro-optic coefficient $r_{33}$, while all other elements of the electro-optic tensor can be neglected. Assuming further that the OEO material in absence of a modulating RF field can be approximated by an isotropic medium with refractive index $n_{\text{OEO}}$, the various matrix multiplications on the right-hand side of (22) can be written in the ($u$, $v$, $w$)-coordinate system as

$$\Delta\boldsymbol{\varepsilon}_{\text{r}}^{(u,v,w)}\left(x,y,z,t'\right) = -n_{\text{OEO}}^4 r_{33}(x,y)\,\mathrm{E}_{\text{RF},w}\left(x,y,z,t'+\frac{z}{v_{\text{g}}}\right)\begin{pmatrix}0&0&0\\0&0&0\\0&0&1\end{pmatrix}, \tag{23}$$

where the superscript ($u$, $v$, $w$) on the left-hand side of the equation indicates that various components of the 3×3 matrix $\Delta\boldsymbol{\varepsilon}_{\text{r}}$ refer to the ($u$, $v$, $w$) coordinate system, while the space dependence is still expressed in terms of ($x$, $y$, $z$). Accordingly, $\mathbf{E}_{\text{RF},w}(x, y, z, t'+z/v_{\text{g}})$ refers to the $w$-component of the electric RF vector field in the ($u$, $v$, $w$) chromophore coordinate system of the OEO material. Note that the electric field $\mathbf{E}_{\text{RF}}(x, y, z, t)$ associated with the modulation signal was already specified in (13) and (14) and referred to the natural time frame $t$ rather than to its retarded counterpart $t' = t - z/v_{\text{g}}$. This transformation needs to be taken into account when deriving $\mathbf{E}_{\text{RF},w}(x, y, z, t' + z/v_{\text{g}})$ from (14) and inserting it into (23).

Inserting (23) into (21), we can express the time-dependent change of the modal propagation constant along z, again using the $w$-component $\underline{\mathcal{E}}_{\text{opt},w}(x,y)$ of the electric field $\underline{\boldsymbol{\mathcal{E}}}_{\text{opt}}(x,y)$ that is associated with the optical mode,

$$\Delta\beta\left(z,t'\right) = -\frac{\omega\varepsilon_0}{4\mathcal{P}_{\text{opt}}}\iint n_{\text{OEO}}^4 r_{33}(x,y)\mathrm{E}_{\text{RF},w}\left(x,y,z,t'+\frac{z}{v_{\text{g}}}\right) \times\left|\underline{\mathcal{E}}_{\text{opt},w}(x,y)\right|^2\mathrm{d}x\,\mathrm{d}y. \tag{24}$$

The $w$-components $\underline{\mathcal{E}}_{\text{opt,w}}(x,y)$ and $\mathrm{E}_{\text{RF},w}(x, y, z, t')$ of the optical mode field and the RF mode field can be obtained by projecting the associated vectorial quantities $\underline{\boldsymbol{\mathcal{E}}}_{\text{opt}}(x,y)$ and $\underline{\boldsymbol{\mathcal{E}}}_{\text{RF}}(x,y)$ on the local $w$-axis of our coordinate system, see Fig. 6(c) for an illustration of the various vectors and their orientations. To this end, we express the DC poling field $\boldsymbol{\mathcal{E}}_{\text{pol}}(x,y)$ by an amplitude $\mathcal{E}_{\text{pol}}(x,y)$ and an associated unit vector $\boldsymbol{e}_{\text{pol}}(x,y)$, which points along the local $w$-axis (poling direction),

$$\boldsymbol{\mathcal{E}}_{\text{pol}}(x,y) = \mathcal{E}_{\text{pol}}(x,y)\;\mathbf{e}_{\text{pol}}(x,y). \tag{25}$$

We further assume that the transverse components of the RF mode field are in phase such that we can also extract a real-valued unit vector $\boldsymbol{e}_{\text{RF}}(x,\ y)$ that points along the local direction of the RF field,

$$\underline{\boldsymbol{\mathcal{E}}}_{\text{RF}}(x,y) = \underline{\mathcal{E}}_{\text{RF}}(x,y)\mathbf{e}_{\text{RF}}(x,y). \tag{26}$$

The same assumption is made for the optical mode fields, leading to a real-valued unit vector $\boldsymbol{e}_{\text{opt}}(x,\ y)$ that indicates the direction of the local electric field associated with the optical mode,

$$\underline{\boldsymbol{\mathcal{E}}}_{\text{opt}}(x,y) = \underline{\mathcal{E}}_{\text{opt}}(x,y)\;\mathbf{e}_{\text{opt}}(x,y). \tag{27}$$

The projection of the transverse electric field associated with the optical and the RF mode onto the poling direction can hence

be simply expressed by dot scalar products of the associated unit vectors or, equivalently, by cosine expressions of the angles between the various vectors, see Fig. 6(c) for an illustration,

$$\begin{aligned}\underline{\mathcal{E}}_{\text{opt},w}(x,y) &= \underline{\mathcal{E}}_{\text{opt}}(x,y)\ \mathbf{e}_{\text{opt}}(x,y)\cdot\mathbf{e}_{\text{pol}}(x,y)\\ &= \underline{\mathcal{E}}_{\text{opt}}(x,y)\ \cos\left(\vartheta_{\text{opt}}(x,y)\right),\end{aligned} \tag{28}$$

$$\begin{aligned}\underline{\mathcal{E}}_{\text{RF},w}(x,y) &= \underline{\mathcal{E}}_{\text{RF}}(x,y)\mathbf{e}_{\text{RF}}(x,y)\cdot\mathbf{e}_{\text{pol}}(x,y)\\ &= \underline{\mathcal{E}}_{\text{RF}}(x,y)\ \cos\left(\vartheta_{\text{RF}}(x,y)\right),\end{aligned} \tag{29}$$

where we introduce the angles $\vartheta_{\text{opt}}(x, y)$ and $\vartheta_{\text{RF}}(x, y)$ between the local poling direction as imposed by the DC poling field and the electrical field of the optical and the RF mode, respectively, see Fig. 6(c). The cosines of $\vartheta_{\text{opt}}(x, y)$ and $\vartheta_{\text{RF}}(x, y)$ are then given by the dot product of the corresponding unit vectors, $\cos(\vartheta_{\text{opt}}(x, y)) = \mathbf{e}_{\text{opt}}(x, y)\cdot\mathbf{e}_{\text{pol}}(x, y)$ and $\cos(\vartheta_{\text{RF}}(x, y)) = \mathbf{e}_{\text{RF}}(x, y)\cdot\mathbf{e}_{\text{pol}}(x, y)$. Introducing (13), (14), (28), and (29) into (24), the time-dependent change of the optical model propagation constant can be expressed as

$$\begin{aligned}\Delta\beta(z,t') &= \Re\left\{-\frac{\pi e^{\mathrm{j}\omega_{\text{RF}}\left(t'+\frac{z}{v_g}\right)}}{\underline{\Pi}_{\text{PM}}}\frac{\underline{U}_{\text{d}}\underline{Z}_{\text{L}}}{\underline{Z}_{\text{L}}+\underline{Z}_{\text{S}}}\frac{e^{-\gamma z}+\underline{\varrho}_{\text{T}}e^{\gamma z}e^{-2\gamma L}}{1-\underline{\varrho}_{\text{S}}\underline{\varrho}_{\text{T}}e^{-2\gamma L}}\right\}\\ &= \Re\left\{-\frac{\pi}{\underline{\Pi}_{\text{PM}}}\underline{U}(z)e^{\mathrm{j}\omega_{\text{RF}}\left(t'+\frac{z}{v_g}\right)}\right\},\end{aligned} \tag{30}$$

where $\underline{U}(z)$ is the complex-valued voltage amplitude at any point $z$ along the transmission line of the SOH PM, while $\underline{\Pi}_{\text{PM}}$ denotes the generalized, frequency-dependent $\pi$-voltage length product of a phase modulator,

$$\begin{aligned}\underline{\Pi}_{\text{PM}} = \Bigg[\iint\limits_{A_{\text{OEO}}}\left(\frac{2\mathcal{P}_{\text{opt}}Z_0\mathcal{U}\lambda}{n_{\text{OEO}}^4 r_{33}(x,y)}\right)^{-1}\underline{\mathcal{E}}_{\text{RF}}(x,y)\left|\underline{\mathcal{E}}_{\text{opt}}(x,y)\right|^2\\ \times\cos^2\left(\vartheta_{\text{opt}}(x,y)\right)\cos\left(\vartheta_{\text{RF}}(x,y)\right)dx\,dy\Bigg]^{-1}\end{aligned} \tag{31}$$

For evaluation of the integral on the right-hand side of (31), we consider the $x$-, and $y$-dependence of $r_{33}(x, y)$ by limiting our integration to the area $A_{\text{OEO}}$ filled with OEO material.

$$r_{33}(x,y) = \begin{cases} r_{33,\text{OEO}} & \text{for } (x,y)\in A_{\text{OEO}}\\ 0 & \text{else}\end{cases}. \tag{32}$$

The complex-valued generalized $U_{\pi,\text{PM}}L$-product $\underline{\Pi}_{\text{PM}}$ as defined in (31) does not only quantify the strength of the interaction between the optical and the RF field, but also considers the phase shift between the locally applied time-harmonic voltage $u(z, t') = \Re\{\underline{U}(z)\ \exp(\mathrm{j}2\pi f_{\text{RF}}t')\}$ at the electrodes and the corresponding local modulation of the local propagation constant $\Delta\beta(z, t') = \Re\{\pi(\underline{U}(z)/\underline{\Pi}_{\text{PM}})\exp(\mathrm{j}2\pi f_{\text{RF}}(t'+z/v_g))\}$ at position $z$. The background of this phase shift can be understood when considering the equivalent-circuit representation of the slot-waveguide transmission line, see Inset (1) of Fig. 1(b). This equivalent circuit corresponds to an $RC$ low-pass, where the local transmission-line voltage $u(z, t')$ is applied to the outer contacts and drops across both, the slot capacitor $C_{\text{sl}}$ and the doped silicon slab resistors. However, only the voltage measured across the capacitor $C_{\text{sl}}$ contributes to the local change $\Delta\varepsilon_{\text{r}}(x,y,z,t')$ of the permittivity and the subsequent modulation $\Delta\beta(z, t')$ of the propagation constant. This leads to a phase lag of the voltage that drop across $C_{\text{sl}}$ with respect to the voltage applied to the outer contacts of the voltage divider, starting at zero for low modulation frequencies $f_{\text{RF}}$ and increasing to $\pi/2$ for $f_{\text{RF}}\to\infty$, while the magnitude of the voltage drop across $C_{\text{sl}}$ continuously decreases with increasing frequency. This is reproduced by numerical simulations of the various mode fields and by extracting the generalized $U_{\pi,\text{PM}}L$-product $\underline{\Pi}_{\text{PM}}$ according to (31): The phase of $\underline{\Pi}_{\text{PM}}$ increases from zero for low modulation frequencies $f_{\text{RF}}$ to $\pi/2$ for $f_{\text{RF}}\to\infty$, while the magnitude of the propagation-constant modulation continuously decreases. In that sense, the complex-valued quantity $\underline{U}_{\pi,\text{PM}} = \underline{\Pi}_{\text{PM}}/L$ can be interpreted as the complex-valued frequency-dependent voltage amplitude, that needs to be applied to a short SOH PM section the generate a phase modulation $\Delta\varphi = L\Delta\beta$ with real-valued amplitude $\pi$, neglecting any impedance mismatch and counterpropagating RF waves, walk-off, and RF losses. In this sense, the generalized $\underline{U}_{\pi,\text{PM}}L$ should be understood as a property of the slot-waveguide cross section, not of the entire device.

Any real device is of course subject to impedance mismatch and resulting partially standing RF waves, walk-off, and RF losses on the PM transmission line. These effects can be quantified by inserting (30) into (20) and by integrating the phase shift along the length of the MZM,

$$\begin{aligned}\varphi_{\text{PM}}(t') &= \Re\Bigg\{-\frac{\pi\underline{U}_{\text{d}}}{\underline{\Pi}_{\text{PM}}}\frac{\underline{Z}_{\text{L}}}{\underline{Z}_{\text{L}}+\underline{Z}_{\text{S}}}\\ &\qquad\times\int_0^L\frac{e^{-\gamma z}+\underline{\varrho}_{\text{T}}e^{\gamma z}e^{-2\gamma L}}{1-\underline{\varrho}_{\text{S}}\underline{\varrho}_{\text{T}}e^{-2\gamma L}}e^{\mathrm{j}2\pi f_{\text{RF}}\left(t'+\frac{z}{v_g}\right)}\,\mathrm{d}z\Bigg\}\\ &= \Re\left\{\underline{\hat{\varphi}}\left(f_{\text{RF}}\right)e^{-\mathrm{j}2\pi f_{\text{RF}}t'}\right\},\end{aligned} \tag{33}$$

where the complex-valued phase-modulation amplitude $\underline{\hat{\varphi}}_{\text{RF}}(f_{\text{RF}})$ contains again both the frequency-dependent decrease of the phase-modulation amplitude and the frequency-dependent phase lag between the applied time-harmonic drive-voltage $u_{\text{S}}(t') = \Re\{\underline{U}_{\text{S}}\ \exp(\mathrm{j}2\pi f_{\text{RF}}t')\}$ applied at the modulator input ($z = 0$) and the associated time-harmonic phase modulation $\varphi(t') = \Re\{\underline{\hat{\varphi}}(f_{\text{RF}})\exp(\mathrm{j}2\pi f_{\text{RF}}t')\}$ measured at the end of the modulator ($z = L$). Note that these time-harmonic oscillations refer to the retarded time $t' = t - z/v_g$. While this does not play a role for the definition of the drive voltage, $t' = t$ for $z = 0$, an additional frequency dependent phase shift $\exp(-\mathrm{j}2\pi f_{\text{RF}}z/v_g)$ would need to be applied to the phase modulation signal at the end $z = L$ of the phase modulator to transfer it back to the natural time frame.

The complex-valued EO transfer function $\underline{D}_{\text{PM}}(f_{\text{RF}})$ of the SOH PM is finally obtained by normalizing the complex-valued frequency-dependent phase-modulation amplitude $\underline{\hat{\varphi}}_{\text{PM}}(f_{\text{RF}})$ measured in the retarded time frame to the value $\underline{\hat{\varphi}}_{\text{PM,id}}(0)$ that would be obtained at zero frequency for an idealized PM having perfectly matched line, source, and termination impedances,

$$\underline{D}_{\text{PM}}(f_{\text{RF}}) = \frac{\underline{\hat{\varphi}}_{\text{PM}}(f_{\text{RF}})}{\underline{\hat{\varphi}}_{\text{PM,id}}(0)}$$

$$= \frac{U_{\pi,PM}L}{\underline{\varPi}_{\text{PM}}} \;\; \underline{B}\left(\frac{e^{\underline{q}^- L}-1}{\underline{q}^-}+\underline{C}\frac{e^{\underline{q}^+ L}-1}{\underline{q}^+}\right). \tag{34}$$

In this relation, the parameters

$$\underline{B} = \frac{2}{L}\frac{\underline{Z}_{\text{L}}}{\underline{Z}_{\text{L}}+\underline{Z}_{\text{S}}}\frac{1}{1-\underline{\varrho}_{\text{S}}\underline{\varrho}_{\text{T}}e^{-2\underline{\gamma}L}} \tag{35}$$

and

$$\underline{C} = \underline{\varrho}_{\text{T}}e^{-2\underline{\gamma}L} \tag{36}$$

account for multiple reflections of the RF wave due to impedance mismatch at the generator and the termination, and the term

$$\underline{q}^{\pm} = \pm\underline{\gamma} + jn_{\text{eg,opt}}\frac{2\pi f_{\text{RF}}}{c} \tag{37}$$

considers RF losses as well as walk-off between the forward-propagating RF field and the optical field ($\underline{q}^+$) as well as the impact of the backward-propagating RF signal portion ($\underline{q}^-$).

Note that the device investigated in the main manuscript is not a simple PM, but a MZM operated in push-pull configuration, where the applied voltage signal simultaneously drives a pair of PM that are configured to produce phase shifts with equal amplitudes but opposite signs in the two MZM arms. As a consequence, the phase difference obtained between the two MZM arms is twice the phase shift of an individual PM, and the generalized $U_\pi L$ product $\underline{\varPi}_{\text{MZM}}$ according to (31) reduces by a factor of two as compared to $\underline{\varPi}_{\text{PM}}$,

$$\underline{\varPi}_{\text{MZM}} = \frac{1}{2}\underline{\varPi}_{\text{PM}}. \tag{38}$$

Despite this difference, the normalized frequency responses of the two devices are identical. To understand this, we consider a push-pull MZM that consists of two identical PM, each operated with a small time-harmonic phase shift of the form $\varphi_{\text{PM}}(t') = \Re\{\underline{\hat{\varphi}}_{\text{PM}}\exp(\text{j}2\pi f_{\text{RF}}t')\} \ll 1 \;\forall\, t'$. The phase difference of the optical signals at the end of the MZM arms is then given by $\varphi_{\text{MZM}}(t') = 2\varphi_{\text{PM}}(t')$, where $\varphi_{\text{PM}}(t')$ can be obtained from (33), and the time-dependent power transfer function can be written as

$$P(t') = P_0\cos^2(\varphi_{\text{b}} + \varphi_{\text{MZM}}(t')), \tag{39}$$

where $P_0$ is the optical output power that the MZM would deliver for full transmission. In case of small-signal modulation $\varphi_{\text{MZM}}(t') \ll 1$ that is imposed on top of a constant bias phase $\varphi_{\text{b}}$, the time-dependent power modulation at the output of the MZM can be written as

$$\begin{aligned} P(t') &\approx P_0\left[\cos^2(\varphi_{\text{b}}) - \varphi_{\text{MZM}}(t')\sin(2\varphi_{\text{b}})\right] \\ &= P_0\cos^2(\varphi_{\text{b}}) - \Re\left\{P_0\underline{\hat{\varphi}}_{\text{MZM}}(f_{\text{RF}})\,e^{j2\pi f_{\text{RF}}t'}\sin(2\varphi_{\text{b}})\right\}. \end{aligned} \tag{40}$$

In the characterization experiment of the MZM, a photodetector is used to convert the MZM output power to an electrical signal, and a subsequent vector network analyzer (VNA) extracts the signal component oscillating at $f_{\text{RF}}$. This component of the MZM output power can again be represented as the real part of an analytic time-domain signal $P_{\text{RF,MZM}}(t') = \Re\{\underline{\hat{P}}_{\text{MZM}}(f_{\text{RF}})\exp(\text{j}2\pi f_{\text{RF}}t')\}$ with the complex-valued power amplitude $\underline{\hat{P}}_{\text{MZM}}(f_{\text{RF}}) = -P_0\underline{\hat{\varphi}}_{\text{MZM}}(f_{\text{RF}})e^{\text{j}2\pi f_{\text{RF}}t'}\sin(2\varphi_{\text{b}})$. The power transfer function of the device can then be defined in analogy to (35)

$$\underline{D}_{\text{MZM}}(f_{\text{RF}}) = \frac{\underline{\hat{P}}_{\text{MZM}}(f_{\text{RF}})}{\underline{\hat{P}}_{\text{MZM,id}}(0)}, \tag{41}$$

where $\underline{\hat{P}}_{\text{MZM,id}}(f_{\text{RF}})$corresponds again to the complex-valued power modulation amplitude that would be obtained at zero frequency for an idealized MZM having perfectly matched line, source, and termination impedances. Inserting (40) into (41) we find

$$\underline{D}_{\text{MZM}}(f_{\text{RF}}) = \underline{D}_{\text{PM}}(f_{\text{RF}}). \tag{42}$$

According to (42), we should be able to compare the simulated transfer function $\underline{D}_{\text{PM}}$ of the PM according to (34) directly to the measured behavior of the SOH MZM. Note, however, that this would require normalization to the transfer characteristics measured at zero frequency for an ideal device having perfectly matched line, source, and termination impedances. Since such a device is not available in practice, and since measurements at zero frequency are generally not reliable due to detector and bias-point drifts, we normalized the measured raw electro-optic transfer function $\underline{D}_{\text{meas,VNA}}$ obtained from our electro-optic vector network analyzer to the value at a sufficiently low reference frequency $f_{\text{ref}} = 70$ kHz, where impedance mismatch, walk-off, and RF losses should not play any role. This leads to the electro-optic transfer function as shown in Fig. 3(c),

$$\underline{S}_{\text{EO,21}}(f_{\text{RF}}) = \frac{\underline{D}_{\text{meas,VNA}}(f_{\text{RF}})}{\underline{D}_{\text{meas,VNA}}(f_{\text{ref}})}. \tag{43}$$

This approach leads to a good agreement of the measured and simulated transfer function, see Fig. 3(c) above.

## Disclosure

Carsten Eschenbaum, Adrian Mertens, and Christian Koos are co-founders of SilOriX GmbH (76131 Karlsruhe, Germany, Registration number: HRB 739782), a startup using silicon-organic hybrid (SOH) technology for commercial applications in different research fields. Adrian Schwarzenberger, Carsten Eschenbaum, Christoph Wilhelm, Stefan Singer, Cheng Feng, Malte Martens, Adrian Mertens, Peter Erk and Christian Koos are employees of SilOriX GmbH.

## References


[1] Epoch AI, "Data on notable AI models," Jul. 2025. Accessed: Jun. 16, 2025, [Online]. Available: https://epoch.ai/data/ai-models

[2] A. Gholami, Z. Yao, S. Kim, C. Hooper, M. W. Mahoney, and K. Keutze, "AI and memory wall," *IEEE Micro*, vol. 44, no. 3, pp. 33–39, May/Jun. 2024, doi: 10.1109/MM.2024.3373763.

[3] S. Y. Siew et al., "Review of silicon photonics technology and platform development," *J. Lightw. Technol.*, vol. 39, no. 13, pp. 4374–4389, Jul. 2021, doi: 10.1109/JLT.2021.3066203.

[4] G. Z. Mashanovich, "Electronics and photonics united," *Nature*, vol. 556, pp. 316–318, 2018, doi: 10.1038/d41586-018-04443-3.

[5] GlobalFoundries Inc., “More compute power, better connectivity: Combining proven CMOS chip fabrication with silicon photonics to move data at the speed of light,” Mar. 7, 2022, Accessed: Jun. 15, 2025. [Online]. Available: gf.com/blog/more-compute-power-better-connectivity-combining-proven-cmos-chip-fabrication-silicon/

[6] A. Ostrovskis et al., “Traveling-wave silicon photonics mach-zehnder modulator for beyond 350 Gb/s transmission in C-band,” presented at the 2025 Opt. Fiber Commun. Conf. Exhib., San Francisco, CA, USA, Mar.–Apr. 2025, Paper M1G.2, doi: 10.1364/OFC.2025.M1G.2.

[7] H. Yamazaki et al., “Net-400-gbps PS-PAM transmission using integrated AMUX-MZM,” *Opt. Exp.*, vol. 27, pp. 25544–25550, 2019, doi: 10.1364/OE.27.025544.

[8] Y. Ogiso et al., “Over 67 GHz bandwidth and 1.5 V $V_\pi$ InP-based optical IQ modulator with n-i-p-n heterostructure,” *J. Lightw. Technol.*, vol. 35, no. 8, pp. 1450–1455, Apr. 2017, doi: 10.1109/JLT.2016.2639542.

[9] M. Nakamura et al., “628 Gb/s net bitrate IMDD transmission using ultrabroadband InP-DHBT-based electrical mixer with upper-sideband gain-enhanced mode,” presented at the 2025 Opt. Fiber Commun. Conf. Exhib., San Francisco, CA, USA, Mar.–Apr. 2025, Paper M3C.3, doi: 10.1364/OFC.2025.M3C.3.

[10] N. Chen, K. Lou, Y. Yu, X. He, and T. Chu, “High-efficiency electro-optic modulator on thin-film lithium niobate with high-permittivity cladding,” *Laser Photon. Rev*, vol. 17, 2023, Art. no. 2200927, doi: 10.1002/lpor.202200927.

[11] C. Wang et al., “Ultrabroadband thin-film lithium tantalate modulator for high-speed communications,” *Optica*, vol. 11, no. 12, pp. 1614–1620, 2024, doi: 10.1364/OPTICA.537730.

[12] K. Powell, X. Li, D. Assumpcao, L. Magalhães, N. Sinclair, and M. Lončar, “DC-stable electro-optic modulators using thin-film lithium tantalate,” *Opt. Exp.*, vol. 32, no. 25, pp. 44115–44122, 2024, doi: 10.1364/OE.538870.

[13] W. Li et al., “Thin-film BTO-based MZMs for next-generation IMDD transceivers beyond 200 gbps/λ,” *J. Lightw. Technol.*, vol. 42, no. 3, pp. 143–1150, Feb. 2024, doi: 10.1109/JLT.2023.3339472.

[14] A. Melikyan et al., “High-speed plasmonic phase modulators,” *Nature Photon.*, vol. 8, pp. 229–233, 2014, doi: 10.1038/nphoton.2014.9.

[15] A. Melikyan et al., “Plasmonic-organic hybrid (POH) modulators for OOK and BPSK signaling at 40 Gbit/s,” *Opt. Exp.*, vol. 23, no. 8, pp. 9938–9946, 2015, doi: 10.1364/OE.23.009938.

[16] S. Ummethala et al., “THz-to-optical conversion in wireless communications using an ultra-broadband plasmonic modulator,” *Nature Photon.*, vol. 13, pp. 519–524, 2019, doi: 10.1038/s41566-019-0475-6.

[17] Y. Horst et al., “Ultra-wideband MHz to THz plasmonic EO modulator,” *Optica*, vol. 12, no. 3, pp. 325–328, 2025, doi: 10.1364/OPTICA.544016.

[18] H. Xu et al., “Ultrahigh performance cross-linkable organic electro-optic material for hybrid modulators,” *Chem. Mater.*, 2025, doi: 10.1021/acs.chemmater.5c00027.

[19] L. Kulmer, T. Blatter, M. Kohli, Y. Horst, S. M. Koepfli, and J. Leuthold, “Single carrier net 400Gbit/s IM/DD over 400m Fiber enabled by Plasmonic Mach-Zehnder modulator,” presented at the Opt. Fiber Commun. Conf. Exhib., San Diego, CA, USA, Mar. 24–28, 2024, Paper W4H.5, doi: 10.1364/OFC.2024.W4H.5.

[20] H. Zwickel et al., “Verified equivalent-circuit model for slot-waveguide modulators,” *Opt. Exp.*, vol. 28, no. 9, pp. 12951–12976, 2020, doi: 10.1364/OE.383120.

[21] A. Schwarzenberger et al., “Silicon-organic hybrid (SOH) mach-zehnder modulator (MZM) for single-carrier IM/DD line rates of 500 gbit/s and beyond,” presented at the 2025 Opt. Fiber Commun. Conf. Exhib., San Francisco, CA, USA, Mar.–Apr. 2025, Paper M4K.1, doi: 10.1364/OFC.2025.M4K.1.

[22] W. Freude et al., “High-performance modulators employing organic electro-optic materials on the silicon platform,” *IEEE J. Sel. Topics Quantum Electron*, vol. 30, no. 4, Jul./Aug. 2024, Art. no. 3400222, doi: 10.1109/JSTQE.2024.3385375.

[23] C. Kieninger et al., “Ultra-high electro-optic activity demonstrated in a silicon-organic hybrid modulator,” *Optica*, vol. 5, no. 6, pp. 739–748, 2018, doi: 10.1364/OPTICA.5.000739.

[24] C. Kieninger et al., “Silicon-organic hybrid (SOH) mach-zehnder modulators for 100 GBd PAM4 signaling with sub-1 dB phase-shifter loss,” *Opt. Exp.*, vol. 28, no. 17, pp. 24693–24707, 2020, doi: 10.1364/OE.390315.

[25] K. F. Lunn and D. Apelian, “Thermal and electrical conductivity of aluminum alloys: Fundamentals, structure-property relationships, and pathways to enhance conductivity,” *Mater. Sci. Eng.: A*, vol. 924, 2025, Art. no. 147766, doi: 10.1016/j.msea.2024.147766.

[26] M. Tan et al., “Co-packaged optics (CPO): Status, challenges, and solutions,” *Front. Optoelectron.*, vol. 16, no. 1, pp. 1–40, 2023, doi: 10.1007/s12200-022-00055-y.

[27] J. X. B. Sia et al., “Wafer-scale demonstration of low-loss (∼0.43 dB/cm), high-bandwidth (>38 GHz), silicon photonics platform operating at the C-band,” *IEEE Photon. J*, vol. 14, no. 3, Jun. 2022, Art. no. 6628609, doi: 10.1109/JPHOT.2022.3170366.

[28] Q. Wilmart et al., “A complete Si photonics platform embedding ultra-low loss waveguides for O- and C-band,” *J. Lightw. Technol.*, vol. 39, no. 2, pp. 532–538, Jan. 2021, doi: 10.1109/JLT.2020.3030123.

[29] W. D. Sacher, Y. Huang, G.-Q. Lo, and J. K. S. Poon, “Multilayer Silicon nitride-on-Silicon integrated photonic platforms and devices,” *J. Lightw. Technol.*, vol. 33, no. 4, pp. 901–910, Feb. 2015, doi: 10.1109/JLT.2015.2392784.

[30] S. Liu et al., “Thermo-optic phase shifters based on silicon-on-insulator platform: State-of-the-art and a review,” *Front. Optoelectron.*, vol. 15, no. 9, pp. 1–21, 2022, doi: 10.1007/s12200-022-00012-9.

[31] Y. Xu et al., “Hybrid external-cavity lasers (ECL) using photonic wire bonds as coupling elements,” *Sci. Rep.*, vol. 11, 2021, Art. no. 16426, doi: 10.1038/s41598-021-95981-w.

[32] M. Lu et al., “Photonic integration using industry ready Photonic wire bonds & facet attached micro-lenses,” *IEEE Trans. Compon., Packag. Manuf. Technol.*, vol. 15, no. 8, pp. 1606–1613, Aug. 2025, doi: 10.1109/TCPMT.2025.3531206.

[33] S. Singer et al., “Linear-drive amplifier-less 112 gbit/s PAM4 operation of a silicon-organic hybrid (SOH) mach-zehnder modulator at 265 mVpp,” *Opt. Exp.*, vol. 33, no. 19, pp. 40055–40074, 2025, doi: 10.1364/OE.551866.

[34] C. Dhote, A. Singh, and S. Kumar, “Silicon photonics sensors for biophotonic applications–A review,” *IEEE Sens. J.*, vol. 22, no. 19, pp. 18228–18239, Oct. 2022, doi: 10.1109/JSEN.2022.3199663.

[35] J. Milivch, D. Kohler, W. Freude, and C. Koos, “Surface sensing with integrated optical waveguides: A design guideline,” *Opt. Exp.*, vol. 26, no. 16, pp. 19885–19906, 2018, doi: 10.1364/OE.26.019885.

[36] IMEC, “Prototyping and low-volume manufacturing of silicon photonic ICs,” Accessed: Jun. 19, 2025, [Online]. Available: https://www.imeciclink.com/en/asic-fabrication/si

[37] AIM Photonics, “Base active PIC,” Accessed: Jun. 19, 2025, [Online]. Available: https://www.aimphotonics.com/base-active-pic

[38] A. Teichler, J. Perelaer, and U. S. Schubert, “Inkjet printing of organic electronics – Comparison of deposition techniques and State-of-the-art developments,” *J. Mater. Chem. C*, vol. 1, no. 10, pp. 1910–1925, 2012, doi: 10.1039/C2TC00255H.

[39] Y. Tominarie, T. Yamada, T. Kaji, C. Yamada, and A. Otomo, “Photostability of organic electro-optic polymer under practical high intensity continuous-wave 1550 nm laser irradiation,” *Jpn. J. Appl. Phys.*, vol. 60, no. 10, pp. 1–25, 2021, doi: 10.35848/1347-4065/ac235a.

[40] A. Mertens, C. Eschenbaum, and C. Koos, “Silicon-organic hybrid slot waveguide modulators on the verge of industrial adoption,” *PICMagazine*, vol. 3, pp. 18–20, 2024.

[41] G. Hong et al., “A brief history of OLEDs—Emitter development and industry milestones,” *Adv. Mater.*, vol. 33, no. 9, 2021, Art. no. 2005630, doi: 10.1002/adma.202005630.

[42] Lightwave Logic Inc., “Lightwave Logic, Inc. Announces perkinamine(TM) polymer reliability breakthrough - passes Telcordia 85/85 test & develops enhanced moisture & oxygen resistance via fourth-generation encapsulation technology,” Jul. 15, 2025. Last access: Sep. 16, 2025. [Online]. Available: accessnewswire.com/newsroom/en/industrial-and-manufacturing/lightwave-logic-inc.-announces-perkinaminetm-polymer-reliability-break-1049059

[43] S. Yokoyama, G. Lu, H. Sato, J. Mao, and A. Bannaron, “Highly reliable organic polymer optical modulators,” in *Proc. 2022 Opt. Fiber Commun. Conf. Exhib.*, 2022, pp. 1–3.

[44] C. Kieninger et al., “Demonstration of long-term thermally stable silicon-organic hybrid modulators at 85 °C,” *Opt. Exp.*, vol. 26, no. 21, pp. 27955–27964, 2018, doi: 10.1364/OE.26.027955.

[45] M. Eppenberger et al., “Resonant plasmonic micro-racetrack modulators with high bandwidth and high temperature tolerance,” *Nature Photon.*, vol. 17, pp. 360–367, 2023, doi: 10.1038/s41566-023-01161-9.

[46] C. Eschenbaum et al., “Thermally stable silicon-organic hybrid (SOH) mach-Zehnder modulator for 140 GBd PAM4 transmission with sub-1 V drive signals,” in *Proc. 2022 Eur. Conf. Opt. Commun.*, 2022, pp. 1–4.

[47] A. Schwarzenberger et al., “First demonstration of a silicon-organic hybrid (SOH) modulator based on a long-term-stable crosslinked electro-optic material,” in *Proc. 49th Eur. Conf. Opt. Commun.*, 2023, pp. 859–862, doi: 10.1049/icp.2023.2357.

[48] *Test Methods Standard Environmental Test methods for Microcircuits*, MIL Standard 883-1, Method 1005.11, 2nd Revision, U.S. Defense Department, Arlington County, VA, USA, 2021.

[49] W. Heni et al., “Nonlinearities of organic electro-optic materials in nanoscale slots and implications for the optimum modulator design,” *Opt. Exp.*, vol. 25, no. 3, pp. 2627–2653, 2017, doi: 10.1364/OE.25.002627.

[50] S. Ummethala et al., “Hybrid electro-optic modulator combining silicon photonic slot waveguides with high-K radio-frequency slotlines,” *Optica*, vol. 8, no. 4, pp. 511–519, 2021, doi: 10.1364/OPTICA.411161.

[51] S. Ummethala et al., “Supplementary document for “Hybrid electro-optic modulator combining silicon photonic slot waveguides with high-K radio-frequency slotlines,” *Optica*, vol. 8, no. 4, pp. 511–519, 2021, doi: 10.6084/m9.figshare.13909739.v3.

[52] Z. Sheng et al., “A compact and CMOS compatible MMI coupler with very low excess loss,” in *Proc. 2013 Opt. Fiber Commun. Conf. Expo. Nat. Fiber Optic Engineers Conf.*, Anaheim, CA, USA, Mar. 17–21, 2013, Paper JTh2A.26, doi: 10.1364/NFOEC.2013.JTh2A.26.

[53] R. Palmer et al., “Low-loss silicon strip-to-slot mode converters,” *IEEE Photon. J.*, vol. 5, no. 1, 2013, Art. no. 2200409, doi: 10.1109/JPHOT.2013.2239283.

[54] A. Kotz et al., “Resistively/capacitively-coupled silicon-organic hybrid (RCC-SOH) Mach–Zehnder modulator offering line rates beyond 400 gbit/s,” presented at the 2025 Conf. Lasers Electro-Opt., Long Beach, CA, USA, May 4–9, 2025, Paper SS187, doi: 10.1364/CLEO_SI.2025.SS187_1.

[55] *IEEE Standard for Ethernet-Amendment 10: Media Access Control Parameters, Physical Layers, and Management Parameters for 200 Gb/s and 400 Gb/s Operation, IEEE Computer Society*, IEEE Standard 802.3bs-2017, Dec. 6, 2017.

[56] Y. Sato, “A method of self-recovering equalization for multi-level amplitude modulation,” *IEEE Trans. Commun.*, vol. 23, no. 6, pp. 679–682, Jun. 1975, doi: 10.1109/TCOM.1975.1092854.

[57] K. Schuh et al., “Single carrier 1.2 tbit/s transmission over 300 km with PM-64 QAM at 100 GBaud,” presented at the 2017 Opt. Fiber Commun. Conf. Exhib., Los Angeles, CA, USA, Mar. 19–23, 2017, Paper Th5B.5, doi: 10.1364/OFC.2017.Th5B.5.

[58] M. Ivanov, C. Häger, F. Brännström, A. Graell i Amat, A. Alvarado, and E. Agrell, “On the information loss of the max-log approximation in BICM systems,” *IEEE Trans. Info. Theory*, vol. 62, no. 6, pp. 3011–3025, Jun. 2020, doi: 10.1109/TIT.2016.2543740.

[59] Q. Hu et al., “Ultrahigh-net-bitrate 363 Gbit/s PAM8 and 279 Gbit/s polybinary optical transmission using plasmonic Mach-Zehnder modulator,” *J. Lightw. Technol.*, vol. 40, no. 10, pp. 3338–3346, May 2022, doi: 10.1109/JLT.2022.3172246.

[60] A. Schwarzenberger et al., “O-band SOH mach-zehnder modulator operating at a PAM4 line rate of 384 Gbit/s with sub-volt drive voltage,” presented at the 2024 Opt. Fiber Commun. Conf. Exhib., San Diego, CA, USA, Mar. 24–28, 2024, Paper Th4B.6, doi: 10.1364/OFC.2024.Th4B.6.

[61] K. Li et al., “Beyond 300Gb/s from an integrated single-channel silicon photonics modulator driver combination,” in *Proc. IEEE SiPhotonics 2024*, 2024, pp. 1/2, doi: 10.1109/SiPhotonics60897.2024.10543408.

[62] M. Xu et al., “Dual-polarization thin-film lithium niobate In-phase quadrature modulators for terabit-per-second transmission,” *Optica*, vol. 9, no. 1, pp. 61–62, 2022, doi: 10.1364/OPTICA.449691.

[63] P. Kharel, C. Reimer, K. Luke, L. He, and M. Zhang, “Breaking voltage–bandwidth limits in integrated lithium niobate modulators using micro-structured electrodes,” *Optica*, vol. 8, no. 3, pp. 357–363, 2021, doi: 10.1364/OPTICA.416155.

[64] Z. Li et al., “Lithium niobate electro-optical modulator based on ion-cut wafer scale heterogeneous bonding on patterned SOI wafers,” *Photon. Res.*, vol. 13, no. 1, pp. 106–112, 2025, doi: 10.1364/PRJ.534954.

[65] O. Marshall, M. Hsu, Z. Wang, B. Kunert, C. Koos, and D. V. Thourhout, “Heterogeneous integration on silicon photonics,” *Proc. IEEE*, vol. 106, no. 12, pp. 2258–2269, Dec. 2018, doi: 10.1109/JPROC.2018.2858542.

[66] N. J. Parsons, A. C. O’Donnell, and K. K. Wong, “Design of efficient and wideband travelling-wave modulators,” in *Proc. Integr. Opt. Circuit Eng. III*, vol. 651, 1986, pp. 148–153, doi: 10.1117/12.938143.

[67] C. Koos, “Nanophotonic devices for linear and nonlinear optical signal processing,” Ph.D. dissertation, Dept. Elect. Eng. Univ.-Verl. Karlsruhe, Karlsruhe, Germany, 2007, doi: 10.5445/KSP/1000007120.